Investigating the quench dynamics of the bound states in a spin-orbital-coupling system using a trapped ion

Hao-Qing Zhang, Ming-Zhong Ai, Jin-Ming Cui, Yong-Jian Han,* Chuan-Feng Li,† and Guang-Can Guo
CAS Key Laboratory of Quantum Information, University of Science and Technology of China, Hefei 230026, China and CAS Center for Excellence in Quantum Information and Quantum Physics, University of Science and Technology of China, Hefei 230026, China

(Received 11 September 2020; accepted 6 August 2021; published 23 August 2021)

The quantum walk, as the quantum analog of the classical random walk, provides a feasible platform to study the topological phenomenon and nonequilibrium dynamics. Here we propose a scheme to realize the quantum walk with a single trapped ion where the Fock states provides the walk space and the zero-phonon state $|n = 0\rangle$ serves as its natural boundary. Thus, our scheme offers an opportunity to investigate the dynamics of the bound states of the corresponding topological systems. In particular, the quench dynamics of the bound states can be extensively studied by tuning the bulk parameters and the local boundary operator, which are experimentally accessible. Our proposal not only offers an alternative approach to exploring the character of the bound states of the topological systems, but also offers a way to determine different phases through the dynamical processes.

DOI: 10.1103/PhysRevA.104.022213

I. INTRODUCTION

Topological matter has been studied extensively on different platforms [1–13]. One of the interesting features is that topological matter is protected by topology against local perturbations, such as the quantization of Hall conduct under impurity [1–4]. Other unique characteristics of topological matter are the appearance of the bound state at the boundary of the sample, for example, the open Su-Schrieffer-Heeger chain in the one-dimensional system [14,15], and the robust chiral edge state moving in one direction at the boundary of the two-dimensional system [16–20]. The bulk topological invariants and the number of bound states can be connected by the bulk-edge correspondence [2,3,21].

Though the equilibrium properties have been widely explored, the nonequilibrium dynamics of the topological system is still under investigation [22–35]. The quench process is the typical nonequilibrium process that has been studied in different topological systems [27,28,36,37]. The bulk topological invariants, such as Chern number, defined in quantum states, are known to be unchanged under unitary dynamics [26,38–40]; thus it is a constant during the quench process. However, the nonunitary processes, such as the dissipation or decoherence process, will change the bulk topological invariants of the states during the quench process [39–41]. Since the bulk-edge correspondence is only valid for the equilibrium situation [40,42–44], the dynamics of the bound states at the boundary of the topological system during nonequilibrium processes is still elusive. For example, Ref. [39] studied quench between topological and nontopological phases in the Haldane model while observing the presence or absence of edge modes. The dynamics of the bound states has attracted a great deal of attention [38]. In addition, how to experimentally observe the dynamics of the bound state is still an open question.

The quantum walk (QW) [45], which can be used to construct universal quantum computation [46–48], has been shown to be a powerful platform to study the equilibrium and nonequilibrium topological properties of spin-orbital-coupling systems [49–63]. In particular, it has been used to observe the bound states [64–66]. Different QWs have been experimentally realized on different platforms, such as photonics [36,37,61,64,65,67,68], neutral atoms [69,70], superconductors [58,71,72], and trapped ions [73,74].

The trapped ion system, which can be accurately controlled and manipulated [75,76], is one of the most ideal platforms for investigating quantum information processing and simulating nonequilibrium dynamics of many-body systems [77–79]. In particular, the QW has been realized in one or two trapped $^{40}Ca^{+}$ ions in the phase space [73,74]. Here we propose to encode the QW onto the Fock states, which is similar to the result in Ref. [80]. The zero-phonon state $|n = 0\rangle$ acts as the natural boundary of the QW. With carefully designed laser sequences, the dynamics of the bound state can be experimentally investigated. We analyze the quench dynamics of the bound state by tuning different parameters in this system.

The paper is organized as follows. In Sec. II we briefly introduce the background of the QW. In Sec. III we discuss how to realize the QW with a boundary in a trapped ion. In Sec. IV the correspondence between boundary operators and the virtual bulk system is introduced. The main results are given in Sec. V. We simulate the formation of the bound state with a scheme to verify the type of bound state. Starting from the built bound state (if any), we study the dynamics of the bound state with quenched QW parameters and how the quench rate affects the edge population. We summarize the results in Sec. VI.

*smhan@ustc.edu.cn
†cfli@ustc.edu.cn

II. QUANTUM-WALK BACKGROUND

A. Introduction to QWs

Quantum walks are quantum versions of the classical random walks. In this paper we focus on the discrete-time quantum walk, which is defined through two operators: the coin-state-dependent shift operation S, which couples the coin state (denoted by $|\uparrow\rangle$ and $|\downarrow\rangle$) and the position state (labeled as $|n\rangle$) of the walker, and the coin operation $R(\theta_n)$ (θ_n is the control parameter, which may depend on the position of the walker n). They are defined as

$$\begin{aligned} S &= \sum_{n=0}^{N-1} |n+1\rangle\langle n| \otimes |\uparrow\rangle\langle\uparrow| + |n\rangle\langle n+1| \otimes |\downarrow\rangle\langle\downarrow|, \\ R(\theta, n) &= \sum_{n=0}^{N-1} |n\rangle\langle n| \otimes e^{-i\sigma_y\theta_n/2}, \end{aligned} \tag{1}$$

where N is the length of the lattice and $\boldsymbol{\sigma} = (\sigma_x, \sigma_y, \sigma_z)$, with σ_k ($k = x, y, z$) the Pauli matrix. The evolution of the QW is governed by the periodic unitary operator $U = SR$; the number of steps of the QW is defined as the number of U operating on the walker. Therefore, the quantum state of the QW after m steps can be obtained by $|\Psi\rangle_m = (SR)^m|\Psi\rangle_0$, where $|\Psi\rangle_0$ is the initial state.

When the coin operator R is independent of the position n and has periodic boundary conditions, the system has translational symmetry. Thus, we can apply the Fourier transform on the position space, that is,

$$\begin{aligned} |n\rangle &= \sum_k e^{-ikn}|k\rangle, \\ S &= \sum_k |k\rangle\langle k| \otimes e^{-ik\sigma_z}, \end{aligned} \tag{2}$$

where $k = 2\pi i/N$ ($i = 0, \ldots, N-1$) and $|k\rangle$ is the quantum state with momentum k. It is clear that the operation S couples the spin and the momentum of the system.

For a general QW with a periodic unitary operator (Floquet operator) U, with the expression of the operators in the momentum space, we can obtain its effective Hamilton as

$$\begin{aligned} U &= e^{-iH_{\text{eff}}}, \\ H_{\text{eff}} &= \sum_k E(k)|k\rangle\langle k| \otimes \mathbf{n}(k)\cdot\boldsymbol{\sigma}. \end{aligned} \tag{3}$$

Here we assume that $t, \hbar = 1$. In addition, $E(k)$ gives the energy dispersion relationship of the system while $n(k) = (n_x(k), n_y(k), n_z(k))$ is the Bloch vector. The effective Hamiltonian is a typical spin-orbital-coupling Hamiltonian, which can display rich topological properties by carefully designing the Floquet operator U.

B. Chiral symmetry and topological phase in one-dimensional split-step QWs

To demonstrate the topological character of the QWs, we focus on the split-step quantum walk [50–54] (SSQW) whose one-step Floquet operator $U(\theta_1, \theta_2)$ is defined as

$$U(\theta_1, \theta_2) = S_+R(\theta_2)S_-R(\theta_1), \tag{4}$$

where

$$\begin{aligned} S_+ &= \sum_{n=0}^{N-1} |n+1\rangle\langle n| \otimes |\uparrow\rangle\langle\uparrow| + |n\rangle\langle n| \otimes |\downarrow\rangle\langle\downarrow|, \\ S_- &= \sum_{n=0}^{N-1} |n\rangle\langle n| \otimes |\uparrow\rangle\langle\uparrow| + |n\rangle\langle n+1| \otimes |\downarrow\rangle\langle\downarrow|, \\ R(\theta_k) &= \sum_{n=0}^{N-1} |n\rangle\langle n| \otimes e^{-i\sigma_y\theta_k/2} \quad (k = 1, 2). \end{aligned} \tag{5}$$

All operators are independent of the position n. Different from the QW in Eq. (1), the shift operator S is split into two shift operators S_+ and S_-, which denote that the walker moves from $|n\rangle$ to $|n+1\rangle$ and $|n-1\rangle$ when the spin is in states $|\uparrow\rangle$ and $|\downarrow\rangle$ and stays at the same position when the spin is in states $|\downarrow\rangle$ and $|\uparrow\rangle$, respectively, and two rotation operators, including two parameters θ_1 and θ_2, which are introduced in one step of the QW. Similarly, the quantum state of the SSQW after m steps can be obtained by $|\Psi\rangle_m = U^m(\theta_1, \theta_2)|\Psi\rangle_0$. Generally, we begin the evolution of the system with a localized product state. The dispersion relation $E(k)$ and the component of the Bloch vector $n(k)$ in its effective Hamiltonian H_{eff} [see Eq. (3)] are calculated as

$$\begin{aligned} \cos E(k) &= \cos\left(\frac{\theta_2}{2}\right)\cos\left(\frac{\theta_1}{2}\right)\cos k - \sin\left(\frac{\theta_1}{2}\right)\sin\left(\frac{\theta_2}{2}\right), \\ n_x(k) &= \frac{\cos\left(\frac{\theta_2}{2}\right)\sin\left(\frac{\theta_1}{2}\right)\sin k}{\sin E(k)}, \\ n_y(k) &= \frac{\sin\left(\frac{\theta_2}{2}\right)\cos\left(\frac{\theta_1}{2}\right) + \cos\left(\frac{\theta_2}{2}\right)\sin\left(\frac{\theta_1}{2}\right)\cos k}{\sin E(k)}, \\ n_z(k) &= -\frac{\cos\left(\frac{\theta_2}{2}\right)\cos\left(\frac{\theta_1}{2}\right)\sin k}{\sin E(k)}. \end{aligned} \tag{6}$$

It can be found that the Bloch vectors are rotating along the $(\cos(\frac{\theta_1}{2}), 0, \sin(\frac{\theta_1}{2}))$ axis in this system when the momentum k ranges from 0 to 2π.

Actually, the quasiequilibrium topology of the QW is strongly related to the symmetry of the system. Chiral symmetry, which is defined as the existence of a unitary operator Γ to satisfy $\Gamma^2 = 1$ and $\Gamma U\Gamma = U^{-1}$ (thus $\Gamma H_{\text{eff}}\Gamma = -H_{\text{eff}}$), is the symmetry in QWs with carefully designed orders of operators. The chiral symmetry defined in the QWs is updated with the development of the QWs. Initially, the chiral symmetry was defined by Kitagaw *et al.* [50] for the Floquet operator in Eq. (5) as $\Gamma_\theta^{-1}U(\theta)\Gamma_\theta = U^{-1}(\theta)$ [which is equal to $\Gamma_\theta^{-1}H_{\text{eff}}(\theta)\Gamma_\theta = -H_{\text{eff}}(\theta)$]. However, the parameter θ dependence of $\Gamma_\theta = e^{-i\pi\mathbf{A}_\theta\cdot\sigma/2}$ is not satisfied and the chiral symmetry of the QWs is later updated to the parameter-independent form [53]. The phase diagram of such a SSQW modified by Eq. (5) can be determined in two different time frames with chiral symmetry (CS) [53] as

$$\begin{aligned} U_1(\theta_1, \theta_2) &= R\left(\frac{\theta_1}{2}\right)S_+R(\theta_2)S_-R\left(\frac{\theta_1}{2}\right), \\ U_2(\theta_1, \theta_2) &= R\left(\frac{\theta_2}{2}\right)S_-R(\theta_1)S_+R\left(\frac{\theta_2}{2}\right), \end{aligned} \tag{7}$$

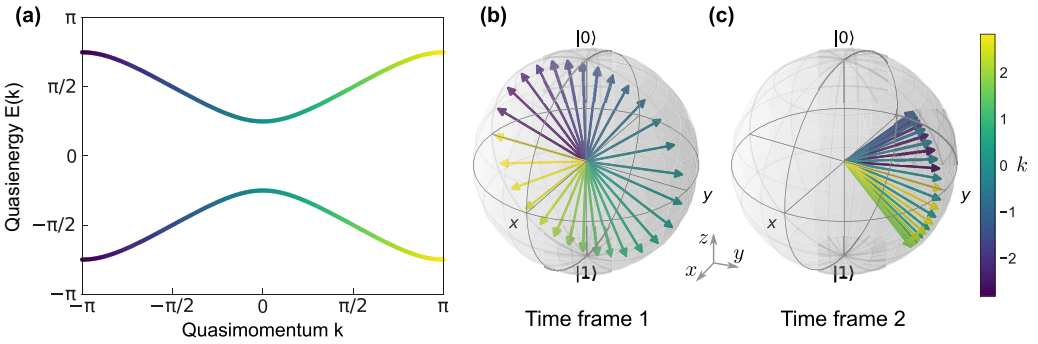

FIG. 1. Split-step quantum walk with the parameters $\theta_1 = \frac{\pi}{2}$ and $\theta_2 = 0$. (a) Dispersion relationship, which is independent of the time frame. (b) and (c) Two time frames with CS to obtain the $\mathbb{Z}_2 \times \mathbb{Z}_2$ topological invariants. In this case, $\nu' = 1$ and $\nu'' = 0$, and thus $\nu_0 = 1$ and $\nu_\pi = 1$ based on Eq. (8)

where $\Gamma = \sigma_x$ (independent of the parameters θ_1 and θ_2), which means that the Bloch vector $n(k)$ of the effective Hamiltonian H_{eff} in U_1 and U_2 rotates along the x axis [51] (see Fig. 1). Strictly, the SSQW defined in Eq. (4) is not chiral symmetrical because its rotation axis is dependent on the parameter θ_1; however, its phase diagram can also be defined through the topological invariants based on Ref. [53]. Actually, the different phases of the SSQW can be identified by a pair of $\mathbb{Z}_2 \times \mathbb{Z}_2$ topological invariants [53], where

$$\begin{aligned} \nu_0 &= \tfrac{1}{2} + \tfrac{1}{2}(\nu' + \nu''), \\ \nu_\pi &= \tfrac{1}{2} + \tfrac{1}{2}(\nu' - \nu''), \end{aligned} \tag{8}$$

where ν_0 (ν_π) is defined as the number of bound states with eigenenergy 0 (π) in the finite-size system and ν' (ν'') is a bulk invariant which is defined as the winding number of the system in the first (second) time frame [37] (see Fig. 1). Thus, Eq. (8) clearly demonstrates the bulk-edge correspondence in the one-dimensional QW system.

According to the bulk-edge correspondence, the bound states will appear at the boundary of the phases with different topologies. Furthermore, the system exhibits particle-hole symmetry (PHS): $\mathcal{P} H_{\text{eff}} \mathcal{P}^{-1} = -H_{\text{eff}}$. Here $\mathcal{P}$ is the complex conjugation operator. One can easily test the property $\mathcal{P} U \mathcal{P}^{-1} = U$ for all the evolution operators R_y where $S_\pm$ are real. The bound state will be protected by PHS [52] and robust against small perturbation. In particular, the vacuum can be viewed as a special phase and the bound states may appear at the boundary of a semifinite (finite) QW system.

III. EXPERIMENTAL PROPOSAL

Trapped ion systems have been proved to be a powerful platform for quantum simulation [76]. Here we propose a way to realize the QW with a boundary by a single $^{171}\text{Yb}^+$ ion in a three-dimensional harmonic trap. In this system, the coin state of the QW is encoded in the $|F = 1, m_F = 0\rangle := |\uparrow\rangle$ and $|F = 0, m_F = 0\rangle := |\downarrow\rangle$ levels of the $^2S_{1/2}$ hyperfine manifold of the $^{171}\text{Yb}^+$ ion with splitting $\omega_{\text{hpf}} = 2\pi \times 12.6$ GHz; the lattice sites of the QW are encoded in the number of phonons, where the zero-phonon state $|n = 0\rangle$ provides the natural boundary of the QW. In order to realize the QW operation as in Eq. (4), the auxiliary Zeeman energy level $|F = 1, m_F = 1\rangle := |a\rangle$ will also be introduced to provide a temporary shelving state. See Fig. 2 for experimental sketches of the proposal.

To realize the QW, we need to implement two different types of basic operators: the rotation operator $R(\theta)$ and the shifting operator $S_\pm$. The rotation operator $R(\theta)$ of the coin in the QW is easy to realize by manipulating the hyperfine states ($|\uparrow\rangle$ and $|\downarrow\rangle$) by microwaves [75,81] or by the stimulated Raman process [75,82]. Implementing the operator $S_\pm$ in the Fock states needs more work and is a bit complicated. Below we will first focus on how to implement $S_\pm$ and then

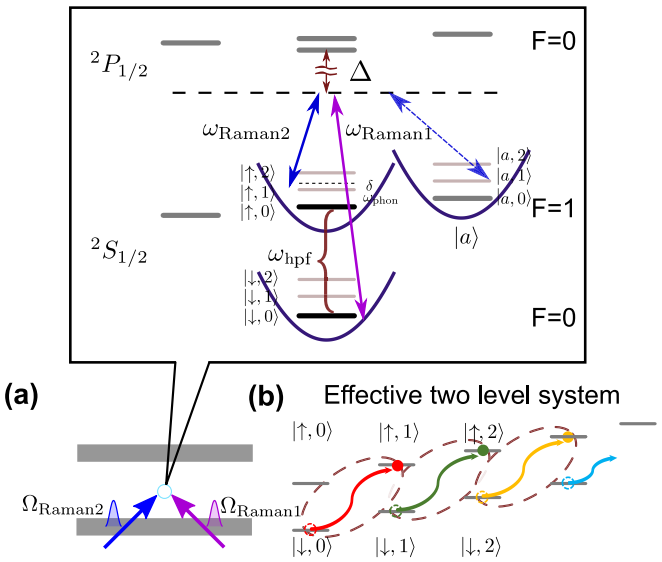

FIG. 2. Experimental sketches. (a) Energy-level diagram of a single trapped $^{171}\text{Yb}^+$ ion. Perpendicular Raman beams are used to excite the axial motional mode. Here $|\uparrow, n\rangle$, $|\downarrow, n\rangle$, and $|a, n\rangle$ represent $|n\rangle \otimes |\uparrow\rangle$, $|n\rangle \otimes |\downarrow\rangle$, and $|n\rangle \otimes |a\rangle$. The auxiliary level $|F = 1, m_F = 1\rangle := |a\rangle$ works for temporal state shelving and it has no occupation after the whole operation. When changing the detuning between the Raman beams, a phonon operation between $|\uparrow\rangle$ and $|\downarrow\rangle$ (blue solid line) or $|a\rangle$ and $|\downarrow\rangle$ (blue dashed line) could be selected. Here $\omega_{\text{Zm}} \gg \omega_{\text{phon}}$ is assumed; thus the motional sideband for different Zeeman levels can be exactly driven. (b) Effective two-level system described by the anti-Jaynes-Cummings model, where $|\uparrow, n+1\rangle$ and $|\downarrow, n\rangle$ are coupled. In our proposal, the Jaynes-Cummings model between $|a, n\rangle$ and $|\downarrow, n+1\rangle$ is also required, but we do not draw it here.

summarize the pulse sequence to realize the whole QW in the phonon space.

To implement $S_{\pm}$, interaction between the hyperfine states ($|\uparrow\rangle$ and $|\downarrow\rangle$) with energy splitting $\omega_{\rm hpf}$ and the phonons with frequency $\omega_{\rm phon}$ is necessary. Generally, this interaction can be realized by a pair of properly selected stimulated Raman beams with frequencies $\omega_{\rm Raman1}$ and $\omega_{\rm Raman2}$ [where $\omega_{\rm Raman1} - \omega_{\rm Raman2} = \omega_{\rm hpf} \pm \omega_{\rm phon} + \delta$, $-$ $(+)$ denotes the red (blue) sideband, and δ is the two-photon detuning]. Under the rotating-wave approximation, the induced interaction can be described by the effective two-level Jaynes-Cummings (JC) and anti-Jaynes-Cummings (AJC) Hamiltonians [83,84]

$$H_{\rm JC} = \eta\frac{\Omega}{2}a^{\dagger}\sigma_{-}e^{i\delta t} + \text{H.c.},$$
$$H_{\rm AJC} = \eta\frac{\Omega}{2}a\sigma_{-}e^{i\delta t} + \text{H.c.}, \tag{9}$$

where $\Omega = \frac{\Omega_{\rm Raman1}\Omega_{\rm Raman2}}{2\Delta}$ is the effective Rabi frequency, with $\Omega_{\rm Raman1}$ and $\Omega_{\rm Raman2}$ denoting the Rabi frequencies which are proportional to the laser intensity of the corresponding Raman beams and Δ the single-photon detuning from the upper $^2P_{1/2}$ excited state; $a^{\dagger} = \sum_{n=0}\sqrt{n+1}|n+1\rangle\langle n|$ is the creation operation of phonon; σ_{+} (σ_{-}) is the flipping operation $|\uparrow\rangle\langle\downarrow|$ ($|\downarrow\rangle\langle\uparrow|$) of spin; and η is the Lamb-Dicke parameter, which is always much smaller than 1.

With this integration, the phonon states $|n\rangle$ (the Fock state with n phonon) can be manipulated. The red sideband beam induces the transition $|n\rangle\otimes|\downarrow\rangle \leftrightarrow |n-1\rangle\otimes|\uparrow\rangle$, with Rabi frequency $\Omega_{n,n-1} = \eta\sqrt{n}\Omega$. We note that $|n\rangle\otimes|\downarrow\rangle$ and $|n-1\rangle\otimes|\uparrow\rangle$ span the nth closed subspace of the JC model. Similarly, the blue sideband beam induces the transition $|n\rangle\otimes|\downarrow\rangle \leftrightarrow |n+1\rangle\otimes|\uparrow\rangle$, with Rabi frequency $\Omega_{n+1,n} = \eta\sqrt{n+1}\Omega$. The states $|n\rangle\otimes|\downarrow\rangle$ and $|n+1\rangle\otimes|\uparrow\rangle$ span the nth closed subspace of the AJC model. Unfortunately, the Rabi frequency $\Omega_{n+1,n}$ is phonon-number dependent, which indicates that we cannot shift all the phonon states (corresponding to the lattice site of the QW) simultaneously. As a result, to implement the hopping operators $S_{\pm}$ homogeneously needs additional effort and is the main obstacle to realizing the QW.

Actually, the homogeneous hopping operator $S_{\pm}$ can be further realized by adiabatic passage, which has already been used to cool the motional state [85–87], and stimulated Raman passage (STIRAP) for phonon arithmetic [88]. Both of the passages are based on the adiabatic theorem [89]: If the beginning state of a quantum system is the ground state of its initial Hamiltonian $H(0)$, when the Hamiltonian of this system changes slowly enough [86] and the ground state of $H(t)$ is well isolated from the others by energy gaps, the system will stay in the ground state of $H(t)$ all the time. In the STIRAP, the time-dependent frequency difference between Raman beams is introduced as $\omega_{\rm Raman1} - \omega_{\rm Raman2} = \omega_{\rm hpf} + \omega_{\rm phon} + \delta(t)$ to adiabatically drive the blue sideband transition between $|\downarrow\rangle$ and $|\uparrow\rangle$, where $\delta(t) = \delta_0\cos(\frac{\pi t}{\tau})$ [88] (δ_0 is the detuning at the initial time and τ is the total evolution time). The effective Rabi frequency is modulated to the time-dependent form $\Omega(t) = \Omega_0\sin(\frac{\pi t}{\tau})$ (also $t\in[0,\tau]$) in the JC and AJC models. Initially $[t=0,\ \delta(t)=\delta_0$, and $\Omega(t)=0]$, the state $|n\rangle\otimes|\downarrow\rangle$ is the ground state of the nth subspace of the initial Hamiltonian of the JC (AJC) model; finally $[t=\tau,\ \delta(\tau)=-\delta_0$, and $\Omega(\tau)=0]$, the state $|n-1\rangle\otimes|\uparrow\rangle$ ($|n+1\rangle\otimes|\uparrow\rangle$) is the ground state of the nth subspace of the final Hamiltonian $H(\tau)$ of the JC (AJC) model. According to the adiabatic theorem, the initial states with different n can adiabatically evolve to their corresponding final states simultaneously and the homogeneous hopping can be realized by this adiabatic process carefully designed above.

According to Ref. [88], to make the previous adiabatic theorem work, the parameters should be selected to satisfy the adiabatic condition; in particular, the minimal gap during the evolution [denoted by $g_{\rm min}(t)$] for any n should satisfy $g_{\rm min}(t) \ll 1/\tau$. Actually, the eigenenergy spectrum can be calculated by $\text{gap}(t) = 2\sqrt{\eta^2(n+1)\Omega(t)^2/4 + \delta(t)^2}$ for each phonon number n, which is plotted in Fig. 3(b) with $\tau = 20\pi/\eta\Omega_0$ and $\delta_0 = 2\eta\Omega_0$. Given a maximal phonon number n_m, δ_0 should be set as $\eta\sqrt{n_m+1}\Omega/2$ (which is the Rabi frequency for the $|n_m\rangle\otimes|\downarrow\rangle \leftrightarrow |n_m+1\rangle\otimes|\uparrow\rangle$ transition).

With the previous method, for the blue sideband operation s_{+} (to distinguish from $S_{\pm}$ in QWs), $|n\rangle\otimes|\downarrow\rangle \to |n+1\rangle\otimes|\uparrow\rangle$ can be realized simultaneously for all the phonon states if the initial state is $|\Psi\rangle = \sum_n c_n|n\rangle\otimes|\downarrow\rangle$, where only spin state $|\downarrow\rangle$ appears. However, when the rotation operator $R(\theta)$ is applied in the system (some terms with spin state $|\uparrow\rangle$ will appear), the initial-state requirement cannot be guaranteed. To solve this problem, we introduce an auxiliary level $|a\rangle$ for state shelving.

When the coin state is mixed by the rotation operation and the auxiliary level is empty (which always can be realized, as detailed in the sixth step of the proposal in the following), the red sideband operation s_{-} (see the second step) adiabatically shelves the quantum state from $|\downarrow\rangle$ to $|a\rangle$. Followed by spin flipping between $|\downarrow\rangle$ and $|\uparrow\rangle$ (see the third step), the phonon state leaves $|\downarrow\rangle$ and $|a\rangle$ in a product state, which satisfies the initial-state requirement of the homogeneous transition s_{+} $|n\rangle\otimes|\downarrow\rangle \to |n+1\rangle\otimes|\uparrow\rangle$. In fact, for the red sideband operation s_{-} (between the spin level $|\downarrow\rangle$ and auxiliary level $|a\rangle$), $|n\rangle\otimes|\downarrow\rangle \to |n-1\rangle\otimes|a\rangle$ can be realized by tuning the frequency difference as $\omega_{\rm Raman1} - \omega_{\rm Raman2} = \omega_{\rm hpf} + \omega_{\rm Zm} - \omega_{\rm phon} + \delta(t)$, where $\omega_{\rm Zm}$ is Zeeman splitting under a magnetic field. In addition, the sideband operation (red and blue) should satisfy the condition $\omega_{\rm Zm} \gg \omega_{\rm phon}$ to address the motional sidebands of $|a\rangle$ while not exciting the motional sidebands of other levels when operating them.

In order to speed up the adiabatic process and suppress the nonadiabatic excitation, the additional counterdiabatic terms in the control are suggested [88]. Further methods to reshape the waveform for shortcut Raman passage have been proposed and realized in experiments [90–93]. With these shortcut methods, the phonon shift speeds up to $\tau = 5\pi/\eta\Omega_0$ (with $\eta = 0.1$ and $\Omega_0 = 2\pi\times 500$ kHz) and we have $\tau = 50$ μs. In the whole six-step proposal, steps 2 and 5 require the STIRAP, which takes up most of the time in the whole six-step procedure. As a result, it is reasonable to estimate the $\tau = 100$ μs operation time for the whole procedure. Thus more than ten steps can be realized during the coherence time with the current technology (as shown in Sec. IV, the number of steps is enough to observe many important physical phenomena).

In our proposal, the Zeeman sublevel is needed for temporal state shelving. By stabilizing the magnetic field, the

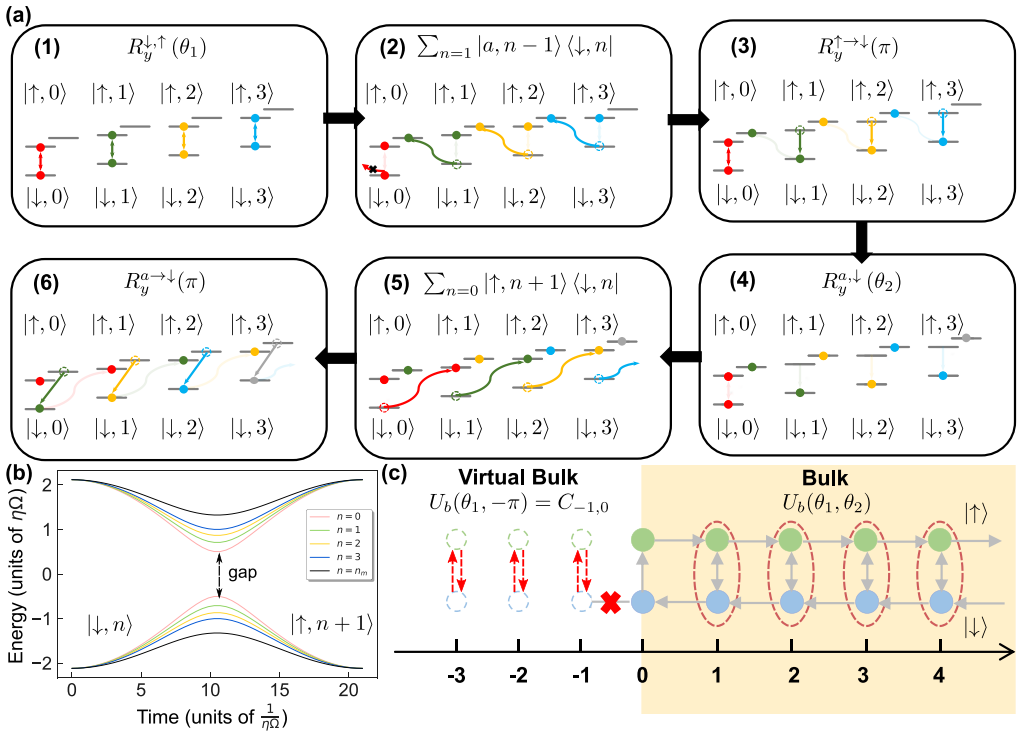

FIG. 3. (a) Pulse sequences to realize a QW within a boundary. Six steps are required to construct $U(\theta_1,\theta_2)$ along the black arrow direction. The first and fourth steps are coin operations which mix the spin states; the other steps are for spin-dependent phonon-number shifting. Here $|0\rangle\otimes|\downarrow\rangle$ is blocked in the second step for the phonon reduction and then flips to $|0\rangle\otimes|\uparrow\rangle$ in the third step. Thus it simulates the spin-flipping operation at the boundary as in Eq. (18). The first four phonon states with the corresponding internal states $|\downarrow\rangle$, $|\uparrow\rangle$, and $|a\rangle$ are shown. Note that there is zero probability to find the ion on the $|a\rangle$ level at the end of the sixth step. (b) Instantaneous eigenenergies of the modulated anti-Jaynes-Cummings model $H(t)$ in the subspace $|n\rangle\otimes|\downarrow\rangle\leftrightarrow|n+1\rangle\otimes|\uparrow\rangle$ (in units of $\eta\Omega_0$). The usable motional quantum number n_m is set equal to 10 and $\delta_0=2\eta\Omega_0$. The operation time $\tau=20\pi/\eta\Omega_0$ to satisfy the adiabatic condition (the evolution is much slower than the timescale set by the energy gap). The whole process then adiabatically transforms the quantum state from $|\downarrow\rangle\otimes|n\rangle$ to $|\uparrow\rangle\otimes|n+1\rangle$ (or $|a\rangle\otimes|n-1\rangle$) for all n. (c) Virtual bulk topological invariant defined with the boundary operation. By introducing the virtual site at the $n=-1$ lattice, we can define the boundary cut link operator $C_{-1,0}$ as mentioned in Eq. (22). Furthermore, the parameter for the virtual bulk phase is also determined.

decoherence due from this source can be ignored. The main limit of the steps should be the phonon coherence time. In the experiment, the phonons are inevitably coupled with the external thermal reservoir and introduce noise, as well as the initial-state preparation error, which is well described by the master equation

$$\dot{\rho}(t)=\frac{\gamma}{2}\bar{n}[2\hat{a}^\dagger\rho(t)\hat{a}-\rho(t)\hat{a}\hat{a}^\dagger-\hat{a}\hat{a}^\dagger\rho(t)]+\frac{\gamma}{2}(\bar{n}+1)[2\hat{a}\rho(t)\hat{a}^\dagger-\rho(t)\hat{a}\hat{a}^\dagger-\hat{a}^\dagger\hat{a}\rho(t)].$$

Here γ denotes the coupling between the phonon and thermal reservoir and $\bar{n}$ denotes the average phonon number for the thermal reservoir. In the experiment of Ref. [88], $\gamma\bar{n}\approx 150$ Hz. The main source of the noise is the electric-field noise from the trapped electrodes. These heating effects could be reduced by operating at low temperatures or cleaning the electrodes.

To complete and help understanding, we provide the unitary operation for each step of the SSQW and give an example of quantum state evolution with the initial state $|\Psi\rangle_0=|0\rangle\otimes|\downarrow\rangle$. Note that we use $s_\pm$ to represent adiabatic sideband operations (to distinguish from $S_\pm$ in the SSQW) and define $\Delta\omega=\omega_{\text{Raman1}}-\omega_{\text{Raman2}}$.

Step 1. Apply rotation $R_y(\theta_1)$ in the spin-state space (spanned by $|\uparrow\rangle$ and $|\downarrow\rangle$), which can be easily realized by two Raman lasers with $\Delta\omega=\omega_{\text{hpf}}$. The evolution operator $R_y^{\downarrow,\uparrow}(\theta_1)$ and the evolution of the state $|\Psi\rangle_0$ are

$$R_y^{\downarrow,\uparrow}(\theta_1)=\sum_{n=0}^{\infty}|n\rangle\langle n|\otimes\left[\cos\left(\frac{\theta_1}{2}\right)(|\uparrow\rangle\langle\uparrow|+|\downarrow\rangle\langle\downarrow|)-\sin\left(\frac{\theta_1}{2}\right)(|\uparrow\rangle\langle\downarrow|-|\downarrow\rangle\langle\uparrow|)+|a\rangle\langle a|\right],$$
$$|\Psi\rangle_1=|0\rangle\otimes\left[\cos\left(\frac{\theta_1}{2}\right)|\downarrow\rangle-\sin\left(\frac{\theta_1}{2}\right)|\uparrow\rangle\right]. \quad (10)$$

They are independent of the number of phonons and the rotation angle θ_1 can be controlled precisely by pulse duration. Note that this operation only mixes $|n\rangle\otimes|\downarrow\rangle$ and $|n\rangle\otimes|\uparrow\rangle$ and leaves $|a\rangle\otimes|\downarrow\rangle$ empty since the population of the auxiliary level $|a\rangle$ is zero in the initial state.

Step 2. Apply the STIRAP for the first red sideband (spanned by $|a\rangle$ and $|\downarrow\rangle$), with the frequency of the two Raman lasers chosen as $\Delta\omega=\omega_{\text{hpf}}+\omega_{\text{Zm}}-\omega_{\text{phon}}+\delta(t)$.

The evolution operator can be effectively written as

$$s_- = -\sum_{n=1}^{\infty}(|n-1\rangle\langle n|\otimes|a\rangle\langle\downarrow| + |n\rangle\langle n-1|\otimes|\downarrow\rangle\langle a|) + \sum_{n=0}^{\infty}|n\rangle\langle n|\otimes|\uparrow\rangle\langle\uparrow| + |0\rangle\langle 0|\otimes(|\downarrow\rangle\langle\downarrow| + |a\rangle\langle a|) \tag{11}$$

and the state of the system evolves to

$$|\Psi\rangle_2 = |\Psi\rangle_1 = |0\rangle\otimes\left[\cos\left(\frac{\theta_1}{2}\right)|\downarrow\rangle - \sin\left(\frac{\theta_1}{2}\right)|\uparrow\rangle\right].$$

Note that $|0\rangle\otimes|\downarrow\rangle$ cannot be driven at this step. The quantum state of $|\downarrow\rangle$ is temporarily stored on $|a\rangle$ and then flips back to $|\downarrow\rangle$ at step 6.

Step 3. Similar to step 1, apply $R_y(\pi)$ in the spin space (spanned by $|\uparrow\rangle$ and $|\downarrow\rangle$). The evolution operator is

$$R_y^{\uparrow\to\downarrow}(\pi) = \sum_{n=0}^{\infty}|n\rangle\langle n|\otimes(|\downarrow\rangle\langle\uparrow| - |\uparrow\rangle\langle\downarrow| + |a\rangle\langle a|) \tag{12}$$

and the state evolves to

$$|\Psi\rangle_3 = -|0\rangle\otimes\left[\cos\left(\frac{\theta_1}{2}\right)|\uparrow\rangle + \sin\left(\frac{\theta_1}{2}\right)|\downarrow\rangle\right].$$

The quantum state $|\uparrow\rangle$ flips to $|\downarrow\rangle$ and it will flip back at step 5 with the blue sideband operation s_+.

Step 4. Apply $R_y(\theta_2)$ in the space spanned by $|a\rangle$ and $|\downarrow\rangle$. Similar to step 1, $\Delta\omega = \omega_{\rm hpf} + \omega_{\rm Zm}$ and the evolution operator is

$$R_y^{a,\downarrow}(\theta_2) = \sum_{n=0}^{\infty}|n\rangle\langle n|\otimes\left[\cos\left(\frac{\theta_2}{2}\right)(|\downarrow\rangle\langle\downarrow| + |a\rangle\langle a|) - \sin\left(\frac{\theta_2}{2}\right)(|\downarrow\rangle\langle a| - |a\rangle\langle\downarrow|) + |\uparrow\rangle\langle\uparrow|\right]. \tag{13}$$

The quantum state evolves to

$$|\Psi\rangle_4 = -|0\rangle\otimes\left[\cos\left(\frac{\theta_1}{2}\right)|\uparrow\rangle + \sin\left(\frac{\theta_1}{2}\right)\cos\left(\frac{\theta_2}{2}\right)|\downarrow\rangle + \sin\left(\frac{\theta_1}{2}\right)\sin\left(\frac{\theta_2}{2}\right)|a\rangle\right].$$

Note here that the rotation operations are between $|\downarrow\rangle$ and $|a\rangle$.

Step 5. Apply the STIRAP for the first blue sideband (spanned by $|\downarrow\rangle$ and $|\uparrow\rangle$) with $\Delta\omega = \omega_{\rm hpf} + \omega_{\rm Zm} + \omega_{\rm phon} + \delta(t)$. The effective evolution operator is

$$s_+ = -\sum_{n=0}^{\infty}(|n+1\rangle\langle n|\otimes|\uparrow\rangle\langle\downarrow| + |n\rangle\langle n+1|\otimes|\downarrow\rangle\langle\uparrow|) + |n\rangle\langle n|\otimes|a\rangle\langle a| \tag{14}$$

and the state evolves to

$$|\Psi\rangle_5 = |0\rangle\otimes\left[-\cos\left(\frac{\theta_1}{2}\right)|\uparrow\rangle + \sin\left(\frac{\theta_1}{2}\right)\sin\left(\frac{\theta_2}{2}\right)|a\rangle\right] + \sin\left(\frac{\theta_1}{2}\right)\cos\left(\frac{\theta_2}{2}\right)|1\rangle\otimes|\uparrow\rangle.$$

At this step, all the quantum states on $|n\rangle\otimes|a\rangle$ and $|0\rangle\otimes|\uparrow\rangle$ remain unchanged.

Step 6. Apply $R_y(\pi)$ (spanned by $|a\rangle$ and $|\downarrow\rangle$) with $\Delta\omega = \omega_{\rm hpf} + \omega_{\rm Zm}$. The evolution operator is

$$R_y^{a\to\downarrow}(\pi) = \sum_{n=0}^{\infty}|n\rangle\langle n|\otimes(-|\downarrow\rangle\langle a| + |a\rangle\langle\downarrow| + |\uparrow\rangle\langle\uparrow|) \tag{15}$$

and the state evolves to

$$|\Psi\rangle_6 = -|0\rangle\otimes\left[\cos\left(\frac{\theta_1}{2}\right)|\uparrow\rangle + \sin\left(\frac{\theta_1}{2}\right)\sin\left(\frac{\theta_2}{2}\right)|\downarrow\rangle\right] + \sin\left(\frac{\theta_1}{2}\right)\cos\left(\frac{\theta_2}{2}\right)|1\rangle\otimes|\uparrow\rangle.$$

The quantum state on the auxiliary level $|a\rangle$ will flip back to $|\downarrow\rangle$ at the end of this step, which leaves $|a\rangle$ empty before the next step. This means there is no probability to detect the ion at the state $|a\rangle$ and no information is leaked after this step.

The whole process is shown clearly in Fig. 3(a). To complete the QW and observe the physical phenomenon, we need to repeat all the steps many times. Obviously, the zero-phonon state $|n=0\rangle$ which provides the boundary in the QW is special (see step 2 above). We can rewrite the evolution operators $U(\theta_1,\theta_2)$ to distinguish the boundary site from the others (note that a minus sign appears because$|\downarrow\rangle\to|\uparrow\rangle\to|\downarrow\rangle$ gains an additional sign) by multiplying the six steps above and simplifying to

$$U_{x>0}(\theta_1,\theta_2) = S^+_{x>0}e^{-i\theta_2\sigma_y/2}S^-_{x>0}e^{-i\theta_1\sigma_y/2}, \tag{16}$$

where

$$S^+_{x>0} = \sum_{n=0}^{\infty}|n\rangle\langle n|\otimes|\downarrow\rangle\langle\downarrow| - |n+1\rangle\langle n|\otimes|\uparrow\rangle\langle\uparrow|,$$
$$S^-_{x>0} = \sum_{n=0}^{\infty}|n\rangle\langle n|\otimes|\uparrow\rangle\langle\uparrow| - |n\rangle\langle n+1|\otimes|\downarrow\rangle\langle\downarrow|; \tag{17}$$

the boundary operator

$$U_{x=0}(\theta_1) = e^{i\phi}|0\rangle\langle 0|\otimes|\uparrow\rangle\langle\downarrow|e^{-i\theta_1\sigma_y/2}. \tag{18}$$

The parameter ϕ could be controlled after the second step in our experimental proposal: Only the $|0\rangle\otimes|\downarrow\rangle$ state has nonzero occupation among all $|\downarrow\rangle$ states. Thus the σ_z operation between $|\downarrow\rangle$ and other energy levels (except $|\uparrow\rangle$ and $|a\rangle$) gives a relative phase for $|n\rangle\otimes|\uparrow\rangle$ compared with other sites. Due to the chiral symmetry and the PHS requirement of the QW, ϕ can only be 0 or π.

We further discuss how to realize a two-dimensional QW [50,65,71,94,95], which could be associated with nontrivial Chern numbers and the more complex Floquet band structure. A single step with two coin operations and two walk operations is

$$U = S_yR(\theta_2)S_xR(\theta_1), \tag{19}$$

where $S_x = \sum_{x,y}|x+1,y\rangle\langle x,y|\otimes|\uparrow\rangle\langle\uparrow| + |x-1,y\rangle\langle x,y|\otimes|\downarrow\rangle\langle\downarrow|$ and $S_y = \sum_{x,y}|x,y+1\rangle\langle x,y|\otimes|\uparrow\rangle\langle\uparrow| + |x,y-1\rangle\langle x,y|\otimes|\downarrow\rangle\langle\downarrow|$, with x and y independent freedoms. In our proposal, two dimensions of the particle propagation can be encoded in two different motional modes of the ion, for example, the axial and radial motional modes with the

resolved frequencies ω_z and ω_r. Additional Raman beams are required to excite the motional modes. Of course, this two-dimensional model has two reflecting boundaries for $x, y \geqslant 0$. A higher-dimensional QW is also possible with more resolved motional modes involved. With this setup, we can investigate the dynamics of the bound state in the topological system.

IV. BOUNDARY AND VIRTUAL BULK PHASE

Based on the bulk-edge correspondence theory, some bound states will appear at the interface of two topologically different bulk phases. In particular, the bound state may appear at the boundary of a finite or semi-infinite topological system, which can be viewed as the interface of the real bulk topological phase and some virtual bulk phase. Interestingly, the virtual bulk phase is only dependent on the local operator of the boundary. To clearly establish the relations among the bound states, the bulk topological invariants, and the boundary condition, we need to define the correspondence between the virtual bulk phases and the local boundary operators.

To establish the correspondence, we map our semi-infinite model to the cut link model suggested in [53]. In the cut link model, the shift operators of the uncut link ($S_{n,n+1}$) and cut link operation ($C_{n,n+1}$) between the sites n and $n+1$ are introduced as

$$\begin{aligned} S_{n,n+1} =& |n\rangle\langle n+1| \otimes |\downarrow\rangle\langle\downarrow| + |n+1\rangle\langle n| \otimes |\uparrow\rangle\langle\uparrow|, \\ C_{n,n+1} =& |n+1\rangle\langle n+1| \otimes |\uparrow\rangle\langle\downarrow| - |n\rangle\langle n| \otimes |\downarrow\rangle\langle\uparrow|. \end{aligned} \tag{20}$$

The standard SSQW in Eq. (4) ($-\infty \leqslant n \leqslant \infty$) could be decomposed with these operators as

$$U(\theta_1, \theta_2) = \sum \left[\cos\left(\frac{\theta_2}{2}\right) S_{n,n+1} + \sin\left(\frac{\theta_2}{2}\right) C_{n,n+1} \right] R(\theta_1). \tag{21}$$

In particular, in the semi-infinite system, the lattice space stops at the $n = 0$ site; however, for convenience, we can still introduce an additional virtual site $n = -1$ as shown in Fig. 3(c). The cut link operator $C_{-1,0}$ serves as the boundary condition and does not affect the evolution of our system. In the following we can see that the operator $C_{-1,0}$, which can be experimentally controlled, plays a key role in the emergence of the bound state.

Similar to Eq. (21) in the standard SSQW model, we can rewrite Eqs. (17) and (18) in the semi-infinite model of our proposal with uncut link and cut link operators. Take $\phi = 0$ as an example:

$$\begin{aligned} U_{b(x>0)}(\theta_1, \theta_2) =& -\sum_{n=0} \left[\cos\left(\frac{\theta_2}{2}\right) S_{n,n+1} + \sin\left(\frac{\theta_2}{2}\right) C_{n,n+1} \right] \\ & \times R(\theta_1), \\ U_{x=0}(\theta_1) =& C_{-1,0} R(\theta_1). \end{aligned} \tag{22}$$

Obviously, $U_{x=0}(\theta_1)$ is directly connected by the operation $C_{-1,0}$.

Comparing the bulk operator $U_b(\theta_1, \theta_2)$ and the boundary operator $U_{x=0}(\theta_1)$, we find that $U_b(\theta_1, \theta_2 = -\pi) = U_{x=0}(\theta_1)$. As a result, the boundary ($n = 0$) can be viewed as the interface of two bulks: One is the real bulk system with the bulk operator $U_b(\theta_1, \theta_2)$ and the other is the virtual bulk system with the bulk operator $U_b(\theta_1, -\pi)$.

With the correspondence of the boundary operator and the virtual bulk operator, we can obtain the phase diagram of the virtual bulk system. The parameter θ_2 has only two values, $-\pi$ (corresponding to $\phi = 0$ in the boundary operator $U_{x=0}$) and π (corresponding to $\phi = \pi$ in the boundary operator $U_{x=0}$), due to the CS requirement. Consequently, the phase diagram of the virtual bulk system includes two lines in Fig. 4(a).

If and only if the virtual bulk system and the real bulk system have different topologies, the bound states can appear. To clearly verify the statement, we prepare the QW system in the state $|0\rangle \otimes |\downarrow\rangle$ and take $\phi = 0$ as an example. The semi-finite system subsequently evolves under the unitary operator $U(\theta_1, \theta_2)$. We first consider the special case with $\theta_1 = \pi/2$ and $\theta_2 = -\pi$ [red star in the phase (0,1) in Fig. 4(a)], where the system evolves as

$$|0\rangle \otimes |\downarrow\rangle \xrightarrow{1} -\frac{1}{\sqrt{2}}(|0\rangle \otimes |\uparrow\rangle + |1\rangle \otimes |\downarrow\rangle) \xrightarrow{2} -|0\rangle \otimes |\downarrow\rangle. \tag{23}$$

It is clear that after two steps the particle returns to its initial state with an additional minus sign, which indicates that the bound state is the eigenstate with eigenvalue $E = \pm\pi/2$ [51,52] [the same $E = \pm\pi/2$ bound state for the pink star in the phase (1,0) and orange square in the phase (0,0)]. In contrast, for the parameters $\theta_1 = \pi/2$ and $\theta_2 = \pi$ [yellow square in the phase (1,1)], similar analyses conclude that the other bound state (eigenstate) with $E = 0, \pi$ exists, i.e.,

$$|0\rangle \otimes |\downarrow\rangle \xrightarrow{1} |0\rangle \otimes \frac{1}{\sqrt{2}}(|\uparrow\rangle + |\downarrow\rangle) \xrightarrow{2} |0\rangle \otimes |\downarrow\rangle. \tag{24}$$

For more general cases, we use the localization probability at the boundary, $P_{\text{edge}} = p_0 + p_1$, where p_0 and p_1 are the probabilities at $n = 0, 1$ sites, respectively [56], as the indicator of the emergence of the bound state. When bound states appear, the probability P_{edge} will be stabilized with a nonzero value along the evolution steps and the stable on-site probability $P_n =_N \langle\Psi|n|\Psi\rangle_N$ ($N \to \infty$) will exponentially decay along with n for the left finite sites, which means that $P_n \propto e^{-n/\lambda}$ and λ is the localization length.

The localization probability P_{edge} after 100 steps vs different parameters is shown in Fig. 4(b). In the left panel of Fig. 4(b), the parameter θ_2 of the virtual bulk system is chosen as $\theta_2 = -\pi$ (we set the control parameter $\phi = 0$ in our experimental proposal), the parameter θ_2 in the real bulk system is set equal to $\pi/2$, and the parameter θ_1 is the same in the virtual and the real bulk system. The results are shown as the cyan curve in Fig. 4(b). We scan the parameter θ_1 in one period. We study in the time frame $R(\frac{\theta_1}{2})S_+R(\theta_2)S_-R(\frac{\theta_1}{2})$, which preserves CS. In this case, the topologies of the real bulk system and the virtual bulk system are always different and subsequently the bound state always exists. We also set $\theta_1 = \pi/2$ (in the real and the virtual bulk system) and scan θ_2 in the real bulk system ($\theta_2 = -\pi$ in the virtual bulk system); the results are shown as the blue curve in Fig. 4(b), from which we can see that there are no bound states in the region $\theta_2 \in [-3\pi/2, -\pi/2]$ for the topology of the real and the virtual bulk system, which are the same. The similar results when we set the parameter θ_2 in the virtual bulk system equal

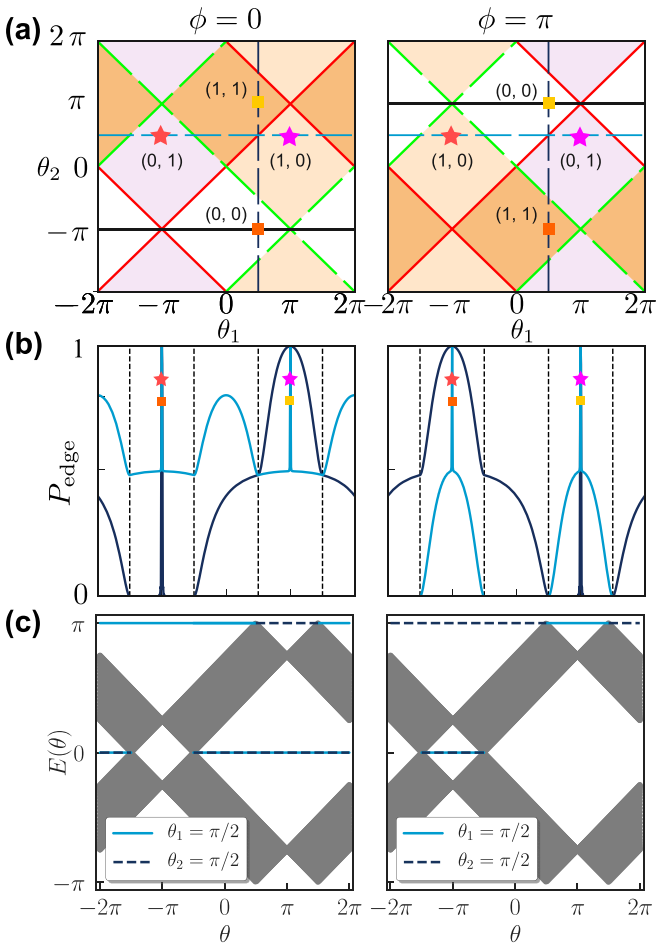

FIG. 4. Phase diagram of the SSQW within a boundary and simulated localization probability at the boundary for different parameters. Here the doublet corresponds to (ν_0, ν_π) in Eq. (8), which characterizes the $\mathbb{Z}_2 \times \mathbb{Z}_2$ topological phase. (a). Phase diagrams of $\phi = 0$ and π (left and right, respectively). The virtual bulk phase (0,0) is defined by the cut link operation $C_{-1,0}$, which corresponds to the region $\theta_2 = -\pi$ (π) for $\phi = 0$ (π) as shown by the black solid line. In the phase diagram, the dashed green lines mean that the gap closes at $E = 0$ and the red solid lines mean that the gap closes at $E = \pi$. The whole diagram is divided into four different phases. (b) Simulation results after 100 steps with $\phi = 0$ and π (left and right diagrams, respectively). The initial state is prepared as $|0\rangle \otimes |\downarrow\rangle$. The appearance of bound states is represented by P_{edge}. The cyan and blue curves correspond to scans over fixed $\theta_1 = \pi/2$ and $\theta_2 = \pi/2$, respectively. A sharp boundary between different regions could be observed for the changing number of bound states $E = 0, \pi$. (c) Real-space energy spectrum $E(\theta)$ with $\phi = 0$ and π (left and right diagrams, respectively), calculated with 100 sites in the system with the boundary operator in Eq. (18). The gray region corresponds to bulk quasienergies and the gaps close at the phase transition points. The cyan solid line corresponds to calculated bound states with fixed $\theta_1 = \pi/2$ and a scan over θ_2; the blue dashed line is for fixed $\theta_2 = \pi/2$ and a scan over θ_1. The appearance of bound states with quasienergy 0 or π coincides with the phase diagram. Note the unique pattern of the Floquet system: The shifting time frame will give the same quasienergy spectrum but a different topological property.

to π are shown on the right-hand side of Fig. 4 (we set the control parameter $\phi = \pi$ in our experimental proposal).

All the calculations are consistent with our observation that the bound states appear if and only if the topology of the virtual bulk is different from that of the real bulk system.

V. DYNAMICS OF BOUND STATES

In the preceding section we verified the existence of bound states when the topologies of the virtual bulk system and the real bulk system are different. In this section we study the dynamics of the bound states. The dynamics of the bound states includes two different situations: One is the dynamics of the formation of the bound states from a local initial state during the evolution; the other is the dynamics of the bound states after the quench of the QW (include quenching parameters of the virtual and the real bulk system). Note that, during the quench process which is unitary, the bulk topological invariant [38,39], such as the winding number [41] or the Chern number [26,38–40], of the quantum state is unchanged. However, we can see that the number of bound states can be changed during the quench.

Unlike the investigation of the quenches in [37], in which the system is prepared as the ground state of Hamiltonian H_0, here the state before the quench is the steady state of a given $U(\theta_1, \theta_2)$ (with or without the boundary state). Actually, in the semi-infinite system, we focus only on the left finite Fock states. The existence of the steady state is justified by the probability $P(x < N_0)$ (N_0 is a given number), particularly $P_{\text{edge}} = p_0 + p_1$. We focus on the time frame $R(\frac{\theta_1}{2})S_+R(\theta_2)S_-R(\frac{\theta_1}{2})$ which preserves CS. When studying the quench of the real bulk system parameters, we control the parameter $\phi = 0$ while changing the rotation angles θ_1 and θ_2 in the experiment. The initial state is always prepared as $|0\rangle \otimes |\downarrow\rangle$.

Here, based on our experimental proposal, we carefully investigate the dynamics of the bound states at the boundary of the semi-infinite QW system. The investigation gives more information about the bulk-edge correspondence in the nonequilibrium process.

A. Formation of the bound state in the semi-infinite QW

We first study the buildup of the bound state when the initial state is prepared as $|0\rangle \otimes |\downarrow\rangle$. We study the dynamics of the system, with the fixed parameter $\theta_2 = -\pi$ $(\phi = 0)$ in the virtual bulk system and the selected rotation angle (θ_1, θ_2) as $(\pi/2, 0)$ [in the phase (1,0)], $(\pi/2, -2\pi/3)$ [in the phase (0,0)] and $(\pi/2, 2\pi/3)$ [in the phase (1,1)] in the real bulk system. To observe the establishment of the bound states, we monitor the evolution of the phonon-state population of the walker in our experimental setup. In Fig. 5(a) the edge population P_{edge} is depicted: It is clear that when the topologies of the real bulk system $(\theta_1 = \pi/2, \theta_2 = -2\pi/3)$ and the virtual bulk system $(\theta_1 = \pi/2, \theta_2 = -\pi)$ are in the same phase (0,0), the population will soon decay to zero (about ten steps in our setup). When there exists a 0-energy (or π-energy) bound state between the virtual and the real bulk system [such as the parameter $(\pi/2, 0)$ shown in Fig. 5(a)], the population will decay and stabilize to about 0.5 in the current situation. However, when there exist two bound states (0 energy and π energy) at the boundary, the edge population will also decay and stabilize to a nonzero value which is bigger than the

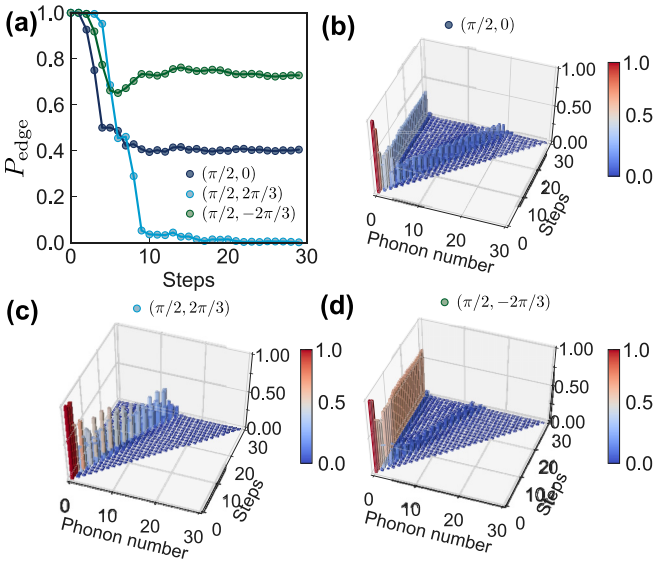

FIG. 5. Existence of a bound state in different regions. We study points in different topologies, $(\pi/2, 0)$ (blue), $(\pi/2, -2\pi/3)$ (cyan), and $(\pi/2, 2\pi/3)$ (green), for the rotation angle in the real bulk system, while in the fixed the virtual bulk system $\theta_2 = -\pi$. The particle is prepared as $|0\rangle \otimes |\downarrow\rangle$. (a) Edge population $P_{\rm edge}$ vs steps. It can be seen that $P_{\rm edge}$ decays to nearly zero after about ten steps when the real bulk system is in the trivial phase. Also shown are plots of the phonon number P_n vs steps in the real bulk system in phases (b) (0,1), (c) (0,0), and (d) (1,1), with the same parameters as in (a). The clear bound states are found at the boundary when the real bulk system is in the nontrivial phase, as expected.

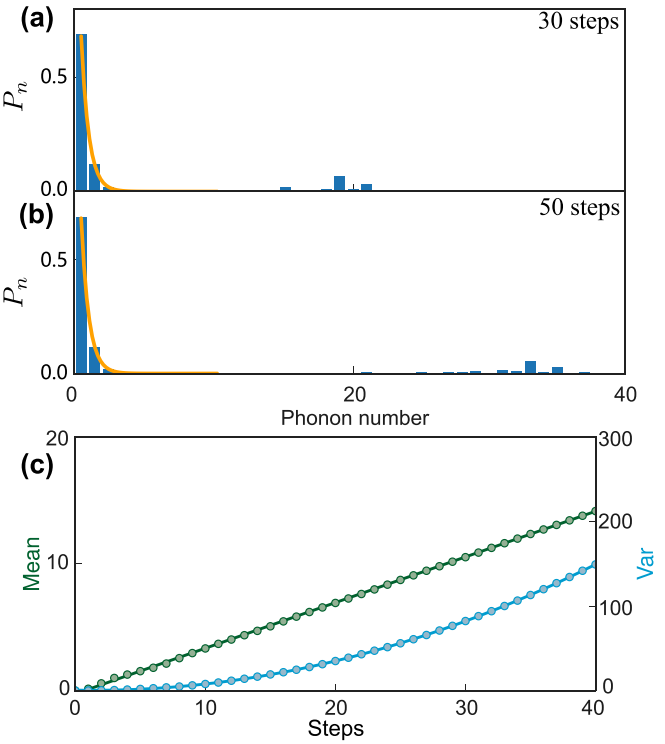

FIG. 6. Simulation result of the phonon-state distribution after (a) 30 and (b) 50 steps, with $\theta_1 = \pi/2$, $\theta_2 = 0$, and $\phi = 0$. A single $E = 0$ bound state appears, as predicted for the real bulk system in the phase (1,0), that has a different topology from the virtual bulk system. The histogram shows the phonon distribution and the orange line is the analytical solution of the eigenstate. (c) Mean and variance of the QW vs steps. The features of the quadratic increment of the deviation and the linear increment of the mean are the patterns of acceleration of the classical random walk.

situation where only one edge mode exists [see in Fig. 5(a)]. From the plot here, we find that the steady bound state is built after ten steps; the different behaviors of $P_{\rm edge}$ are clearly observed for different topological phases. So it is reasonable to observe the formulation of the bound state according to the present experimental ability.

We further fit the stable value of the population distribution of the phonon state in Fig. 6; it can be well described by the exponential decay. The topology of the real bulk system $(\theta_1 = \pi/2, \theta_2 = 0)$ [blue curve in Fig. 5(a)] in the phase (1,0) is different from that of the virtual bulk system $(\theta_1 = \pi/2, \theta_2 = -\pi)$. For this condition, we solve for the eigenstate of evolution operator [51] and analytically find the localization length as $\lambda = 1/\log(\sqrt{2} - 1)$. The simulation results are given in Figs. 6(a) and 6(b) for the evolution after 30 and 50 steps, respectively. The orange curve shows the exponential decay with the localization length λ mentioned above. We find that the fitting is pretty good. In particular, p_1/p_0 and p_2/p_1 are exactly equal to $e^{-2/\lambda}$ during the evolution. We notice that the right-moving bulk state contributes to the increase of the mean and variation of the phonon distribution after each step as in Fig. 6(c).

Here we would like to discuss how to experimentally verify different bound states appearing in the previous situations. Without loss of generality, we set $\phi = 0$ in our simulation and suppose that the bound state $|\psi_b\rangle$ is the eigenstate of the evolution operator $U_{x\geqslant 0}$, i.e.,

$$U_{x\geqslant 0}|\psi\rangle = e^{-iE}|\psi\rangle, \tag{25}$$

with eigenenergy E. Generally, the quantum state of the system after m steps can be written as $|\psi\rangle_m = \sum_n [a_n(m)|\uparrow\rangle + b_n(m)|\downarrow\rangle] \otimes |n\rangle$, where both $a_n(m)$ and $b_n(m)$ are real due to PHS. When the bound state is built, it is stable, that is, $|\psi\rangle_m = |\psi\rangle_{m+1}$ for $E = 0$, while $|\psi\rangle_m = -|\psi\rangle_{m+1}$ for $E = \pi$, where $|\psi\rangle_m$ is the wave function after m steps (m is large enough). We focus only on the evolution of the parameters a_0 and b_0 located on the boundary, i.e.,

$$\begin{aligned} U(\theta_1,\theta_2)\begin{pmatrix} a_0(N) \\ b_0(N) \end{pmatrix} &\to R\left(\frac{\theta_1}{2}\right)\begin{pmatrix} \sin\left(\frac{\theta_1}{2}\right)a_0(N) + \cos\left(\frac{\theta_1}{2}\right)b_0(N) \\ \sin\left(\frac{\theta_2}{2}\right)\left[\cos\left(\frac{\theta_1}{2}\right)a_0(N) - \sin\left(\frac{\theta_1}{2}\right)b_0(N)\right] - \cos\left(\frac{\theta_2}{2}\right)\left[\sin\left(\frac{\theta_1}{2}\right)a_1(N) + \cos\left(\frac{\theta_1}{2}\right)b_1(N)\right] \end{pmatrix} \\ &= \begin{pmatrix} a_0(N+1) \\ b_0(N+1) \end{pmatrix}. \end{aligned} \tag{26}$$

With the stable conditions $a_0(N) = a_0(N+1)$ and $b_0(N) = b_0(N+1)$, we obtain

$$a_0 = \begin{cases} b_0 & \text{for } E = 0 \\ -b_0 & \text{for } E = \pi, \end{cases} \tag{27}$$

which is independent of the parameters θ_1 and θ_2 (however, the existence, the type of bound states, and the localization length are dependent on the parameters). As a result, when the bound state is the 0-energy (π-energy) type, the spin state of the walker at the boundary is $|+\rangle = \frac{1}{\sqrt{2}}(|\uparrow\rangle + |\downarrow\rangle)$ [$|-\rangle = \frac{1}{\sqrt{2}}(|\uparrow\rangle - |\downarrow\rangle)$] or $\langle\sigma_x\rangle = 1$ ($\langle\sigma_x\rangle = -1$). Consequently, the 0- and π-energy bound states are orthogonal and can be directly verified by measuring the operator σ_x. The expectation values of σ_x are easy to measure in trapped ions, by first applying the Hadamard transform of the spin state and then measuring the ion fluorescence.

In Fig. 7 we simulate the evolution of the spin state (at $n = 0, 1$ sites) in the different real bulk systems with the stable bound state. In Fig. 7(a) the rotation angles of the real bulk systems $(\pi/2, \pi/4)$ [in the phase (1,0)] and $(-\pi/2, \pi/4)$ [in the phase (0,1)] have topologies different from those of the virtual bulk system [$(\pi/2, -\pi)$ and $(-\pi/2, -\pi)$]. The red (blue) line for the 0-energy (π-energy) bound state stabilizes to $|+\rangle$ ($|-\rangle$). In contrast, for $(\pi/4, 3\pi/8)$ [in the phase (1,1)], we find instead of stabilizing to a fixed state, the spin state oscillates between two spin states $(a|+\rangle + b|-\rangle$ and $a|+\rangle - b|-\rangle$ for the two adjacent steps), which corresponds to a fixed $\langle\sigma_x\rangle$ between -1 and 1 as in Fig. 7(b).

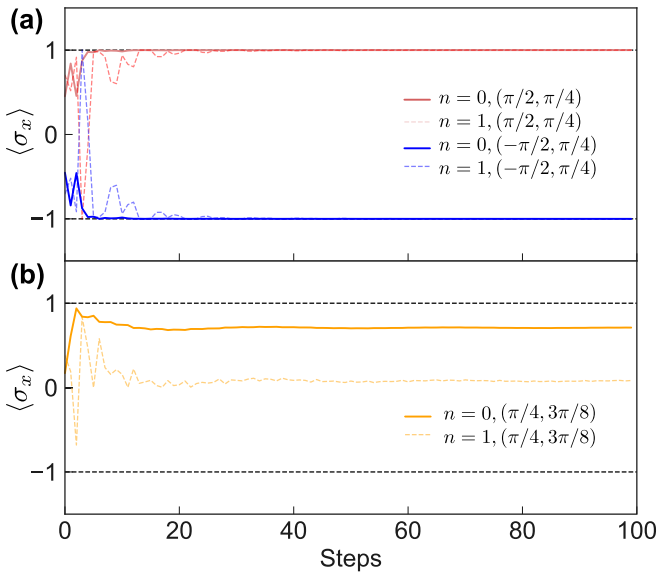

FIG. 7. Verified phases with the spin state of the quantum state $|\psi\rangle_N$. The particle is prepared as $|0\rangle \otimes |\downarrow\rangle$ and evolves after 100 steps. (a) Spin-state space evolution for the system with a single bound state ($E = 0, \pi$) and $n = 0, 1$ sites. Red (blue) lines correspond to a single 0-energy (π-energy) bound state. The average value of σ_x stabilizes to 1 (-1). (b) Spin-state space evolution for the (1,1) system as the superposition of 0- and π-energy bound states. The average value of σ_x stabilizes to a value between 1 and -1, as expected, which is different for $n = 0, 1$ sites

In conclusion, we can easily verify the existence of the bound states by the edge population of the Fock states and further determine the type of bound states by the average value of σ_x in the spin-state space: $\langle\sigma_x\rangle = 1$ for the 0-energy bound state, $\langle\sigma_x\rangle = -1$ for the π-energy bound state, and $-1 < \langle\sigma_x\rangle < 1$ for the superposition of the 0-energy and π-energy bound states. The 0- and π-energy bound states are product state $|\phi_s\rangle \otimes |\phi_p\rangle$, where $|\phi_s\rangle$ is the quantum state in the spin-state space and $|\phi_p\rangle$ is the quantum state with an exponential decay population distribution in the position space. Furthermore, it can be seen clearly in Fig. 7 that $\langle\sigma_x\rangle$ tends to be steady after ten steps and different behavior is associated with topological properties of the bulk system. Thus it is reasonably observed based on current experimental ability.

B. Dynamics of bound states in quenches of QWs

Now we turn to study the dynamics of the bound state in the quench processes. We study the sudden quench of rotation angles in the experiment and thus the real bulk system. The control parameter is set as $\phi = 0$. Initially, the real bulk system is chosen as (θ_1^i, θ_2^i) and the parameters of the virtual bulk system are $(\theta_1^i, -\pi)$. As mentioned before, if the real and virtual bulk systems have different topologies, the bound states will appear. After establishing the bound state by the N_0-step evolution from the initial state $|0\rangle \otimes |\downarrow\rangle$, the rotation angle in the experiment changes at the $N+1$ step, which means the real bulk system suddenly quenches to (θ_1^f, θ_2^f) [the parameter of the virtual bulk system quenches to $(\theta_1^f, -\pi)$ simultaneously]. Then the whole system evolves with these new parameters. Obviously, the existence of the new bound states is strongly dependent on the parameters θ_1^f and θ_2^f. Here we focus only on the dynamics of the bound states by monitoring their edge population P_{edge} still with the left finite Fock states and the expectation value $\langle\sigma_x\rangle$ with the zero-phonon state $|n = 0\rangle$.

First, the initial rotation parameters of the real bulk system are $(3\pi/4, \pi/4)$ [in the phase (1,0)] and those of the virtual bulk system are $(3\pi/4, -\pi)$ [in the phase (0,0)], as shown in Fig. 8(a). Because the real and virtual bulk systems have different topologies, after evolving $N_0 = 20$ steps, a 0-energy bound state appears and becomes stable. Then we change the rotation angles at 21 steps and thus the real bulk system suddenly quenches to different phases and the virtual bulk system stays in the phase (0,0). In Fig. 8(b) the real bulk system quenches to $(\pi/2, \pi/4)$, which is still in the phase (1,0) (a 0-energy bound state exists in the corresponding static system), and the virtual bulk system quenches to $(\pi/2, -\pi)$. As a result, the bound state will be preserved without oscillation and decay. In Fig. 8(c) the real bulk system quenches to $(\pi/8, \pi/4)$, which is in the phase (1,1), and the virtual bulk system quenches to $(\pi/8, -\pi)$. We can see in Fig. 8(b) that the edge population P_{edge} will oscillate, decay, and stabilize to a new value in the end, which indicates the survival of the 0-energy bound state.

To clarify, we further monitor the spin dynamics of the zero-phonon state to determine the type of bound state (0 energy or π energy). As in Fig. 8(f), after stabilization of the edge population, $\langle\sigma_x\rangle = 1$ (0-energy bound state), i.e., the spin state of the bound state tends to be $|+\rangle$, indicating that the

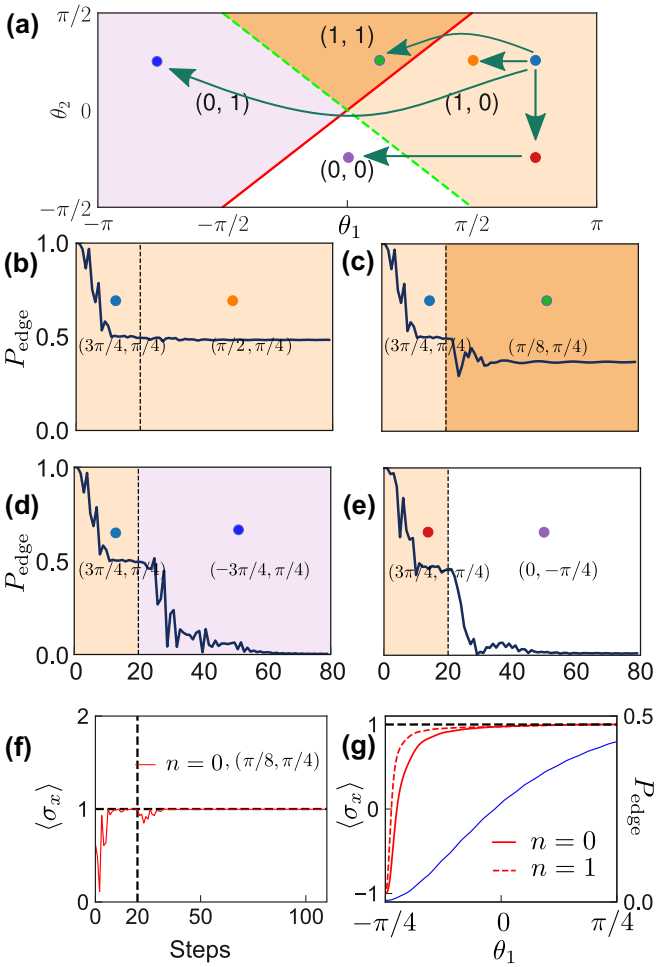

FIG. 8. Quench dynamics starting from the (1,0) phase. The particle is prepared as $|0\rangle \otimes |\downarrow\rangle$. After the first $N_0 = 20$ steps for building the bound state, the real bulk system suddenly quenches to another phase. (a) Parameters we study before and after the quench for the real bulk system. Also shown is the edge population $P_{\rm edge}$ vs evolution steps with the final real bulk system in the phases (b) (1,0), (c) (1,1), (d) (0,1), and (e) (0,0). We note that in all these cases, only the parameters after the quench in the phases (1,1) and (1,0) have the nonzero bound state preserved. (f) Spin-state dynamics at the $n = 0$ site with the same parameters as in (c): First a single 0-energy bound state with $\langle\sigma_x\rangle = 1$ is built at $N_0 = 20$ steps, then it oscillates, and finally it stabilizes to $\langle\sigma_x\rangle = 1$. (g) Expectation value $\langle\sigma_x\rangle$ and edge population $P_{\rm edge}$ vs $\theta_1^f \in [-\pi/4, \pi/4]$ and fixed $\theta_2^f = \pi/4$, which ensures that the system is in the phase (1,1) after the quench.

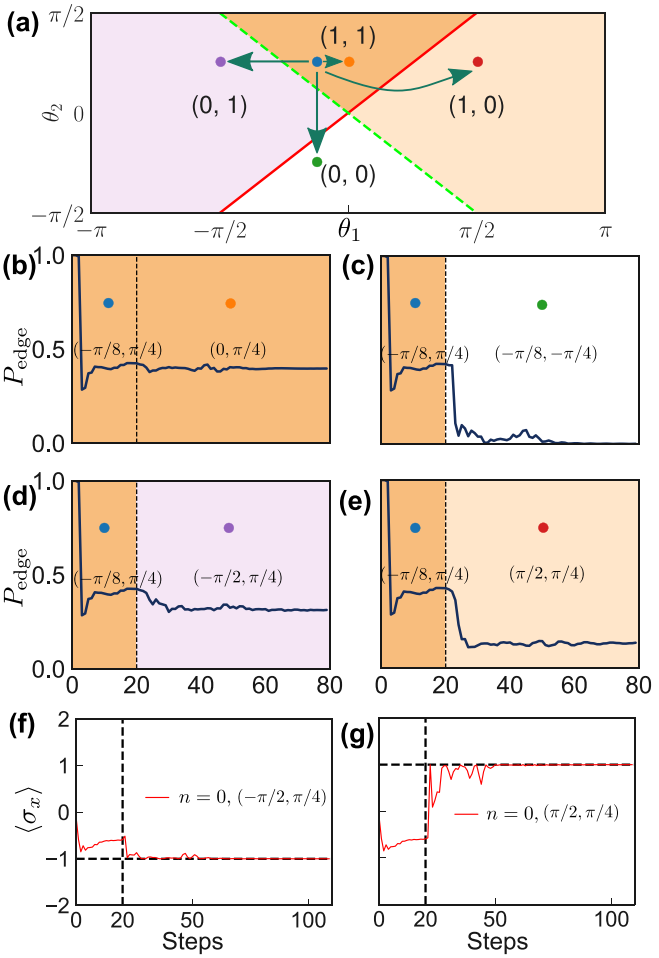

FIG. 9. Quench dynamics starting from the (1,1) phase. The particle is prepared as $|0\rangle \otimes |\downarrow\rangle$. After the first $N_0 = 20$ steps for building the bound state the real bulk system suddenly quenches to another phase. (a) Parameters we study before and after the quench for the real bulk system. Also shown is the edge population $P_{\rm edge}$ vs evolution steps with the final real bulk system in the phases (b) (1,1), (c) (0,0), (d) (1,0), and (e) (0,1). The bound can be preserved except for the system in the phase (0,0) after the quench. (e) and (f) Spin-state dynamics at the $n = 0$ site with the same parameters after the quench as in (c) and (d), respectively. The spin state stabilizes to $|+\rangle$ ($|-\rangle$), which shows a single 0-energy (π-energy) bound state.

bound state is 0 energy. After the real bulk system quenches to the phase (1,1), the expectation value $\langle\sigma_x\rangle$ is still equal to 1, which indicates that the bound state is 0 energy. Figure 8(g) shows $\langle\sigma_x\rangle$ (red curve) and $P_{\rm edge}$ (blue curve) vs the parameters $(\theta_1, \pi/4)$ after quench. Here $\theta_1 \in [-\pi/4, \pi/4]$ to ensure that the real bulk system after quench is in the phase (1,1).

In Fig. 8(d) the real bulk system quenches to $(-3\pi/4, \pi/4)$, which is in the phase (0,1), and the virtual bulk system is in the phase $(-3\pi/4, -\pi)$. A single π-energy bound state will exist with the same parameters after the quench. In contrast, in Fig. 8(e) the real bulk system quenches to $(0, \pi/4)$, which is in the phase (0,0), and the virtual bulk system is in the phase $(0, -\pi)$. Under these two conditions mentioned above, we see that the edge population $P_{\rm edge}$ will oscillate and finally decay to zero.

Second, we study the quench process starting from the establishment of the bound state with the real bulk system $(-\pi/8, \pi/4)$ [in the phase (1,1)] and the virtual bulk system $(-\pi/8, -\pi)$. Both the 0-energy and π-energy bound states can exist before the quench. The superposition of the 0-energy and π-energy bound states can be verified by $\langle\sigma_x\rangle \neq 1$ in Figs. 9(e) and 9(f). Then the real bulk system quenches to a different phase, while the virtual bulk system is still in the phase (0,0). In Fig. 9(a) the parameter of the real bulk system quenches to $(\pi/8, \pi/4)$ [also in the phase (1,1)] and the virtual bulk system is in $(\pi/8, -\pi)$. The bound state will

be preserved after the quench dynamics and the population P_{edge} are almost the same.

In Fig. 9(b) the parameter of the real bulk system quenches to $(-\pi/8, -\pi/4)$, which is in the phase (0,0), and the virtual bulk system is in the phase $(-\pi/8, -\pi)$. Generally, there is no bound state in the quenched static system since the real and virtual bulk systems have the same topology. We can see that the bound state will quickly decay and disappear (the edge population soon decays to zero). In Figs. 9(c) and 9(d) the real bulk system quenches to $(-\pi/2, \pi/4)$ [in the phase (0,1)] and $(\pi/2, \pi/4)$ [in the phase (1,0)] and the virtual bulk system is in the phases $(-\pi/2, -\pi)$ and $(\pi/2, -\pi)$, respectively. We can see the survival of the bound state for the above conditions.

To see the details of the surviving bound states, we monitor their spin dynamics [see Figs. 9(e) and 9(f)]. We find that the expectation value $\langle\sigma_x\rangle$ approaches 1 and -1 in Figs. 9(e) and 9(f), which indicates that only the 0-energy and π-energy bound states survive, respectively, and the other bound state decays in this situation.

Third, we study the initial real bulk system in the phase (0,0) with $(0, -\pi/4)$ and the virtual bulk system also in the phase (0,0) with $(0, -\pi)$. There is no bound state in this system and the edge population will approach 0 after the system evolves $N_0 = 20$ steps. The real bulk system quenches to a different phase and the virtual bulk system stays in the phase (0,0): In Fig. 10(a) the real bulk system quenches to the phase (0,0) with the parameters $(0, -\pi/8)$, in Fig. 10(b) the real bulk system quenches to the phase (1,0) with the parameters $(\pi/2, -\pi/4)$, in Fig. 10(c) the real bulk system quenches the phase (0,1) with the parameters $(-\pi/2, -\pi/4)$, and in Fig. 10(d) the real bulk system quenches to the phase (1,1) with the parameters $(0, \pi/4)$. For all the cases above, the bound state can be established.

Finally, we consider the quench of the virtual bulk system and keep the real bulk system parameters unchanged. As mentioned before, when the real bulk system is set as (θ_1, θ_2), the virtual bulk system also can be controlled (tuned by the parameter ϕ). As shown in Fig. 11(a), the parameter ϕ in the virtual bulk system before quench is set equal to 0. The system supports the nontrivial bound state if the real bulk system (θ_1, θ_2) has a topology different from that of the virtual bulk system. After stabilization of the edge population (with enough evolution steps, $N_0 = 20$ in our simulation), the parameter ϕ of the virtual bulk system suddenly quenches to π. Then the system evolves with the parameter after the quench. We notice that with fixed (θ_1, θ_2) and a quench control parameter ϕ from 0 to π, the original phases (1,0) and (0,1) quench to (0,1) and (1,0), respectively, and the original phases (1,1) and (0,0) quench to (0,0) and (1,1), respectively.

In Fig. 11(b) [Fig. 11(c)] the real bulk system is chosen in the phase (1,0) with the parameters $(3\pi/4, \pi/4)$ [in the phase (0,1) with the parameters $(-3\pi/4, \pi/4)$] and the virtual bulk system is initially in the phase (0,0). There is a 0-energy (π-energy) bound state located between these two bulk systems. After the quench, the real bulk system is in the phase (0,1) [(1,0)] and the quenched virtual bulk system is in $(3\pi/4, 0)$ $[(-3\pi/4, 0)]$. The quenched real and virtual bulk systems still have different topologies. The edge population P_{edge} further evolves to a stable value.

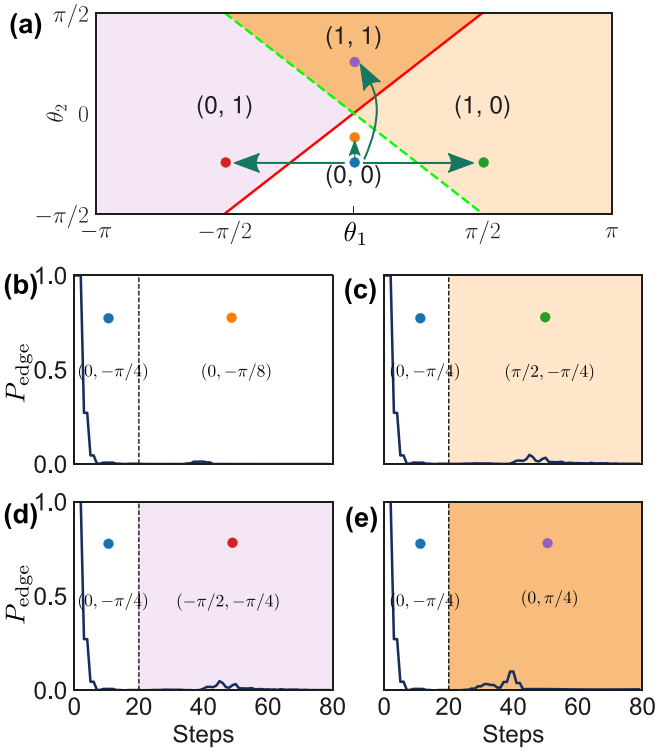

FIG. 10. Quench dynamics starting from the (0,0) phase. The particle is prepared as $|0\rangle \otimes |\downarrow\rangle$. After the first $N_0 = 20$ steps, the real bulk system suddenly quenches to another phase. (a) Parameters we study before and after the quench for the real bulk system. Also shown is the edge population P_{edge} vs evolution steps with the final real bulk system in the phases (b) (1,1), (c) (0,0), (d) (1,0), and (e) (0,1). We note that no bound state can be built when the system is in the phase (0,0) before the quench.

Similarly, we monitor the spin dynamics in Fig. 11(e) [Fig. 11(f)] to see the details of the surviving bound states in Fig. 11(a) [Fig. 11(b)]. We find that the $\langle\sigma_x\rangle$ keep 1 (-1) in Fig. 9(e) [Fig. 9(f)] unchanged. That is because the single 0-energy (π-energy) bound state for $\phi = 0$ before the quench becomes a π-energy (0-energy) bound state for $\phi = \pi$ after the quench, which can be maintained in the system all the time.

In Fig. 11(d) the real bulk system is in the phase (1,1) with the parameters $(-\pi/8, \pi/4)$ and the virtual bulk system is also initially in the phase (0,0) with the parameters $(-\pi/8, -\pi)$. The 0- and π-energy bound states will be stable at the boundary. The virtual bulk system will quench to the original phase (1,1) with the parameters $(-\pi/8, 0)$. The quenched virtual and the real bulk systems have the same topology and there is no bound state. Therefore, the bound state is quickly decays and disappears. In Fig. 11(e) the real bulk system is in the phase (0,0) with the parameters $(0, \pi/4)$ and the virtual bulk system is also in the phase (0,0) with the parameters $(0, -\pi)$. They have the same topology and there is no bound state stable at the boundary. Similarly, the virtual bulk system will quench to the original phase (1,1) and has a topology different from that of the real bulk system; however, the bound state cannot be established in this situation.

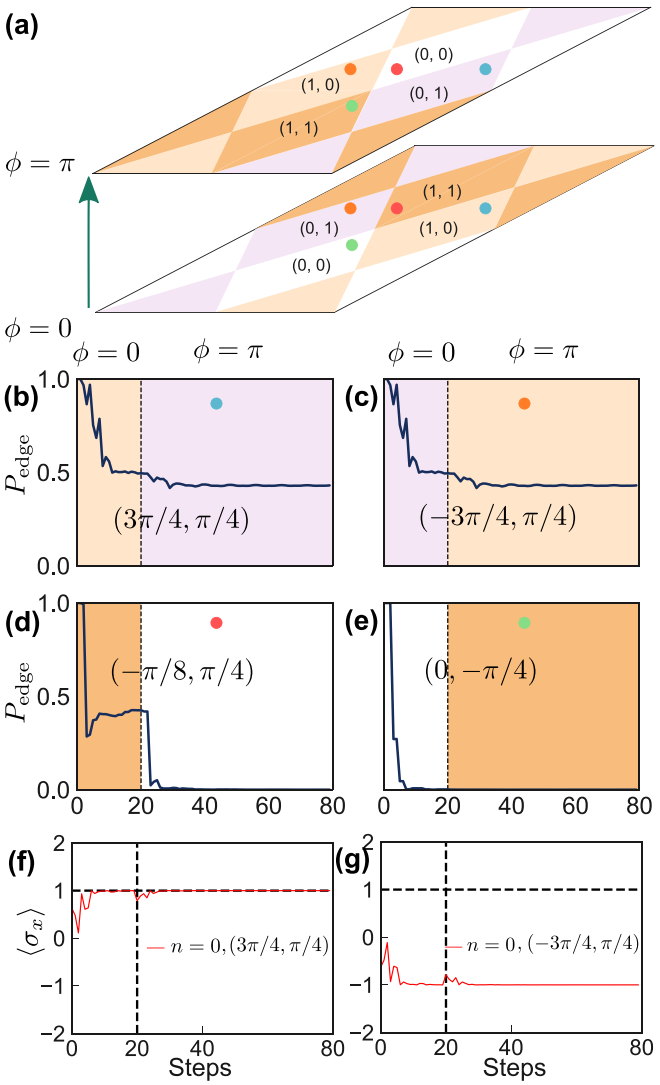

FIG. 11. Quench dynamics of the virtual bulk system. The particle is prepared as $|0\rangle \otimes |\downarrow\rangle$. (a) Diagram of quench in the virtual bulk system. The system first evolves under the control parameter $\phi = 0$ for $N_0 = 20$ steps and then suddenly quenches ϕ to π and thus quenches the virtual bulk system. Also shown is the edge population P_{edge} vs evolution step system before the quench in the phases (b) (1,0), (c) (0,1), (d) (1,1), and (e) (0,0) and the system after the quench in the phases (b) (0,1), (c) (1,0), (d) (0,0), and (e) (1,1). We note that in (b) and (c) the bound states are preserved, and further study spin-state dynamics under these two conditions in (e) and (f).

With the previous simulation results, we find that only when both systems, before and after the quench, support the same type of bound state, the bound state can exist after the quench.

In addition, we find that the 0-energy and π-energy bound states have similar Fock state distributions; however, they have different spin states when they are located at the boundary. Consequently, we can transfer the bound state with a very simple operation: implementing σ_z on site 0. As shown in Fig. 12(a), the blue curve with the σ_z operation has a nonvanishing edge population P_{edge} compared with the purple curve. The spin dynamics in Fig. 12(b) further enhances our

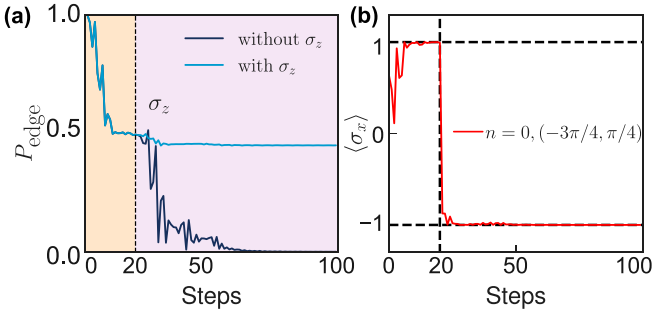

FIG. 12. Recovery of the bound state when the quench is between (1,0) and (0,1) with the same parameters as in Fig. 8(d). (a) Edge population P_{edge} vs evolution steps with and without σ_z operation at the end of step N_0, which transfers $|+\rangle$ to $|-\rangle$ and thus helps recover the bound state. (b) Spin-state dynamics with the additional σ_z operation. We note how a π-energy bound state is built starting from a 0-energy bound state.

argument. First, the spin state of the bound state tends to be $|+\rangle$, which indicates that the 0-energy bound state is built, and then with σ_z the operation swaps $\langle\sigma_x\rangle$ with -1 (thus $|-\rangle$). Then the bound state can further evolve and becomes stable in the phase (0,1).

C. Edge population with different quench rates

We further investigate the relation between the value of P_{edge} and the quench rate. To clearly describe the effect of the quench rate, the initial parameter θ^i quenches to the final parameter θ^f by step N_q and the time-dependent parameter θ^i has the form

$$\theta(t) = \begin{cases} \theta^i, & t < N_0 \\ \theta^i + \frac{\theta^f - \theta^i}{N_q}(t - N_0), & N_0 \leqslant t \leqslant N_0 + N_q \\ \theta^f, & t > N_0 + N_q. \end{cases} \tag{28}$$

The first N_0 steps are used to build the bound state (if any) between the real bulk system with the parameters (θ_1^i, θ_2^i) and the virtual bulk system with the parameters $(\theta_1^i, -\pi)$. Then N_q steps are used to quench the real bulk system and the quench speed $v = \frac{\theta^f - \theta^i}{N_q}$. Obviously, the larger N_q is, the slower the quench dynamics happen. Finally, additional steps (after $N_0 + N_q$ steps) are used to build the bound state (if any) between the real bulk system with the parameters (θ_1^f, θ_2^f) and the virtual bulk system with the parameters $(\theta_1^f, -\pi)$. In this case, we investigate only the relation between P_{edge} and the quench rate. All the proposals mentioned above can be realized precisely in the experiment by changing the rotation angles during each cycle.

In Fig. 13 we study the quench dynamics with different quench steps N_q. All of the quenches are from the real bulk system in the phase (1,0) with the parameters $(\pi/8, \pi/4)$ to the phase (1,1) with the parameters $(3\pi/4, \pi/4)$, and the virtual bulk system is in the phase (0,0). We thus have quench speed $v_q = \frac{5\pi}{8N_q}$. In the initial system, a single 0-energy bound state can be stabilized after $N_0 = 20$ steps since the topologies of the real and virtual bulk systems are different. In Fig. 13(b) we study the edge population vs evolution steps.

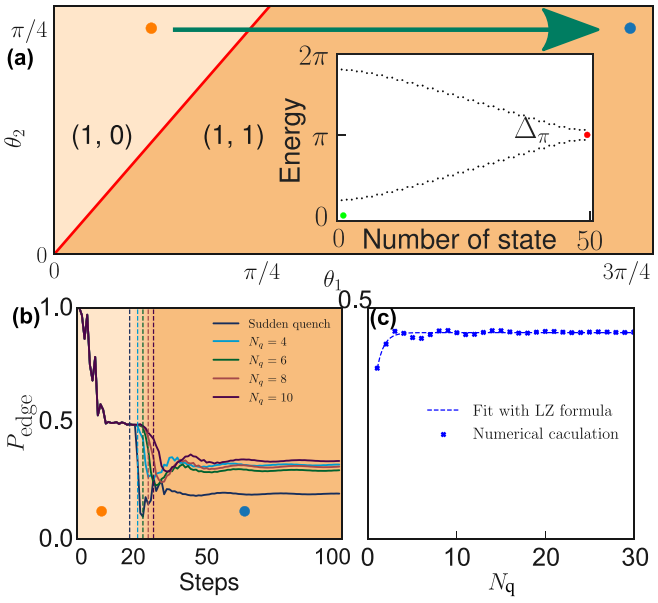

FIG. 13. Quench dynamics starting from the (1,0) phase with different quench steps N_q. The particle is prepared as $|0\rangle \otimes |\downarrow\rangle$. (a) Parameters we study before and after the quench for the real bulk system [same as in Fig. 8(c)]. The inset shows the calculated real-space energy spectrum, with 50 lattice sites under the boundary condition in Eq. (18). The red dot is for the $E = 0$ bound state and the green dot is for the $E = \pi$ bound state. The energy gap Δ_π at $E = \pi$ sets the quench step scale jumping to the π-energy bound state. (b) Edge population P_{edge} vs evolution steps with different N_q. (c) Stable state edge population P_{edge} after the quench. Blue points show the numerical calculation, while the blue dashed line shows the result with the Landau-Zener (LZ) formula, which has the form $e^{-\beta N_q}$ in our condition. Here β is set equal to 1.3.

Blue curves are for the sudden quench ($N_q = 1$), cyan curves are for $N_q = 4$, green curves are for $N_q = 6$, red curves are for $N_q = 8$, and purple curves are for $N_q = 10$. We can see that the population P_{edge} is bigger when the quench is slower. When the quench is slow enough, P_{edge} is almost the same as the P_{edge} before the quench, which indicates that there is no transport happening. However, when the quench is quick, the population decays. This phenomenon can be well understood by the Landau process [96]. The bound state is isolated from the transport modes with a gap as shown in the Fig. 11(a) inset. If the quench is fast, the isolated bound state has some probability of jumping to the transport modes; however, if the quench is slow enough, the process is almost adiabatic and the bound mode cannot jump to the transport modes. To further understand this process, we fit the population P_{edge} vs N_q, which can be well described by the Landau process as $e^{-\alpha \Delta_\pi^2 / v_q}$ (thus $e^{-\beta N}$) in Fig. 13(a). Intuitively, when $v_q < \Delta_\pi$, there will be a limited possibility of jumping to the π-energy bound state. Here $v_q = \frac{5\pi}{8N_q} = \Delta_\pi$ gives $N_q \approx 10$, which coincides with Fig. 13(c); for $N_q > 10$, P_{edge} is almost the same as the P_{edge} before the quench.

VI. CONCLUSION

In this paper we have presented a proposal to realize QWs in the Fock state with a carefully designed laser sequence in a trapped ion. In this proposal, the properties and the dynamics of the bound states can be experimentally observed with a natural boundary. In particular, the quench dynamics of the bound states with energy 0 or π can be monitored by the population of the phonon states and the expectation value of the operator $\langle \sigma_x \rangle$ of the selected internal level of the ion.

Different quench dynamics have been comprehensively discussed. With the development of the manipulation of the phonons [88] in a trapped ion, all the required techniques are available. Actually, all the phenomena associated with the formulation of the bound states can be observed in the experiment based on the analysis in the text. Furthermore, the detection method we proposed does not require any density of state reconstruction, which does not set a limit when more steps can be realized. However, for the quench dynamics we discussed, first steady bound states should be discussed and then the parameters of the system are tuned. The steady-state behavior can be observed at around 20 steps, but the results are still promising with a further increase of the phonon coherence time and phonon operation ability.

[1] K. von Klitzing, Rev. Mod. Phys. **58**, 519 (1986).
[2] M. Z. Hasan and C. L. Kane, Rev. Mod. Phys. **82**, 3045 (2010).
[3] X.-L. Qi and S.-C. Zhang, Rev. Mod. Phys. **83**, 1057 (2011).
[4] H. L. Stormer, D. C. Tsui, and A. C. Gossard, Rev. Mod. Phys. **71**, S298 (1999).
[5] Y. Ando, J. Phys. Soc. Jpn. **82**, 102001 (2013).
[6] Z. Wang, Y. Chong, J. D. Joannopoulos, and M. Soljačić, Nature (London) **461**, 772 (2009).
[7] L. Lu, J. D. Joannopoulos, and M. Soljačić, Nat. Photon. **8**, 821 (2014).
[8] L. Lu, J. D. Joannopoulos, and M. Soljačić, Nat. Phys. **12**, 626 (2016).
[9] T. Ozawa, H. M. Price, A. Amo, N. Goldman, M. Hafezi, L. Lu, M. C. Rechtsman, D. Schuster, J. Simon, O. Zilberberg, and I. Carusotto, Rev. Mod. Phys. **91**, 015006 (2019).
[10] M. Aidelsburger, M. Atala, S. Nascimbène, S. Trotzky, Y.-A. Chen, and I. Bloch, Phys. Rev. Lett. **107**, 255301 (2011).
[11] M. Aidelsburger, M. Atala, M. Lohse, J. T. Barreiro, B. Paredes, and I. Bloch, Phys. Rev. Lett. **111**, 185301 (2013).
[12] N. R. Cooper, J. Dalibard, and I. B. Spielman, Rev. Mod. Phys. **91**, 015005 (2019).
[13] N. Goldman, J. C. Budich, and P. Zoller, Nat. Phys. **12**, 639 (2016).
[14] R. Jackiw and C. Rebbi, Phys. Rev. D **13**, 3398 (1976).
[15] W. P. Su, J. R. Schrieffer, and A. J. Heeger, Phys. Rev. Lett. **42**, 1698 (1979).
[16] K. Nakada, M. Fujita, G. Dresselhaus, and M. S. Dresselhaus, Phys. Rev. B **54**, 17954 (1996).
[17] P. Roulleau, F. Portier, D. C. Glattli, P. Roche, A. Cavanna, G. Faini, U. Gennser, and D. Mailly, Phys. Rev. Lett. **100**, 126802 (2008).
[18] M. Atala, M. Aidelsburger, M. Lohse, J. T. Barreiro, B. Paredes, and I. Bloch, Nat. Phys. **10**, 588 (2014).

[19] M. Mancini, G. Pagano, G. Cappellini, L. Livi, M. Rider, J. Catani, C. Sias, P. Zoller, M. Inguscio, M. Dalmonte, and L. Fallani, Science **349**, 1510 (2015).

[20] B. Stuhl, H.-I. Lu, L. Aycock, D. Genkina, and I. Spielman, Science **349**, 1514 (2015).

[21] M. S. Rudner, N. H. Lindner, E. Berg, and M. Levin, Phys. Rev. X **3**, 031005 (2013).

[22] M. Heyl and J. C. Budich, Phys. Rev. B **96**, 180304(R) (2017).

[23] M. Heyl, Rep. Prog. Phys. **81**, 054001 (2018).

[24] J. C. Budich and M. Heyl, Phys. Rev. B **93**, 085416 (2016).

[25] C. Yang, L. Li, and S. Chen, Phys. Rev. B **97**, 060304(R) (2018).

[26] C. Wang, P. Zhang, X. Chen, J. Yu, and H. Zhai, Phys. Rev. Lett. **118**, 185701 (2017).

[27] N. Fläschner, D. Vogel, M. Tarnowski, B. Rem, D.-S. Lühmann, M. Heyl, J. C. Budich, L. Mathey, K. Sengstock, and C. Weitenberg, Nat. Phys. **14**, 265 (2018).

[28] M. Tarnowski, F. N. Ünal, N. Fläschner, B. S. Rem, A. Eckardt, K. Sengstock, and C. Weitenberg, Nat. Commun. **10**, 1728 (2019).

[29] M. G. Floquet, Ann. Sci. École Norm. Super. **12**, 47 (1883).

[30] J. H. Shirley, Phys. Rev. **138**, B979 (1965).

[31] M. Grifoni and P. Hänggi, Phys. Rep. **304**, 229 (1998).

[32] F. Wilczek, Phys. Rev. Lett. **109**, 160401 (2012).

[33] S. Choi, J. Choi, R. Landig, G. Kucsko, H. Zhou, J. Isoya, F. Jelezko, S. Onoda, H. Sumiya, V. Khemani, C. von Keyserlingk, N. Y. Yao, E. Demler, and M. D. Lukin, Nature (London) **543**, 221 (2017).

[34] J. Rovny, R. L. Blum, and S. E. Barrett, Phys. Rev. Lett. **120**, 180603 (2018).

[35] J. Berges, S. Borsányi, and C. Wetterich, Phys. Rev. Lett. **93**, 142002 (2004).

[36] X.-Y. Xu, Q.-Q. Wang, S.-J. Tao, W.-W. Pan, Z. Chen, M. Jan, Y.-T. Zhan, K. Sun, J.-S. Xu, Y.-J. Han, C.-F. Li, and G.-C. Guo, Phys. Rev. Research **1**, 033039 (2019).

[37] X.-Y. Xu, Q.-Q. Wang, M. Heyl, J. C. Budich, W.-W. Pan, Z. Chen, M. Jan, K. Sun, J.-S. Xu, Y.-J. Han, C.-F. Li, and G.-C. Guo, Light: Sci. Appl. **9**, 7 (2020).

[38] L. D Alessio and M. Rigol, Nat. Commun. **6**, 8336 (2015).

[39] M. D. Caio, N. R. Cooper, and M. J. Bhaseen, Phys. Rev. Lett. **115**, 236403 (2015).

[40] Y. Hu, P. Zoller, and J. C. Budich, Phys. Rev. Lett. **117**, 126803 (2016).

[41] M. McGinley and N. R. Cooper, Phys. Rev. Lett. **121**, 090401 (2018).

[42] L. Zhang, L. Zhang, S. Niu, and X.-J. Liu, Sci. Bull. **63**, 1385 (2018).

[43] Y. Wang, W. Ji, Z. Chai, Y. Guo, M. Wang, X. Ye, P. Yu, L. Zhang, X. Qin, P. Wang, F. Shi, X. Rong, D. Lu, X.-J. Liu, and J. Du, Phys. Rev. A **100**, 052328 (2019).

[44] C.-R. Yi, L. Zhang, L. Zhang, R.-H. Jiao, X.-C. Cheng, Z.-Y. Wang, X.-T. Xu, W. Sun, X.-J. Liu, S. Chen, and J.-W. Pan, Phys. Rev. Lett. **123**, 190603 (2019).

[45] Y. Aharonov, L. Davidovich, and N. Zagury, Phys. Rev. A **48**, 1687 (1993).

[46] A. M. Childs, Phys. Rev. Lett. **102**, 180501 (2009).

[47] A. M. Childs, D. Gosset, and Z. Webb, Science **339**, 791 (2013).

[48] R. Portugal, *Quantum Walks and Search Algorithms* (Springer, New York, 2013).

[49] M. C. Banuls, C. Navarrete, A. Perez, E. Roldan, and J. C. Soriano, Phys. Rev. A **73**, 062304 (2006).

[50] T. Kitagawa, M. S. Rudner, E. Berg, and E. Demler, Phys. Rev. A **82**, 033429 (2010).

[51] T. Kitagawa, Quantum Inf. Process. **11**, 1107 (2012).

[52] J. K. Asbóth, Phys. Rev. B **86**, 195414 (2012).

[53] J. K. Asbóth and H. Obuse, Phys. Rev. B **88**, 121406(R) (2013).

[54] J. K. Asbóth, B. Tarasinski, and P. Delplace, Phys. Rev. B **90**, 125143 (2014).

[55] H. Obuse, J. K. Asbóth, Y. Nishimura, and N. Kawakami, Phys. Rev. B **92**, 045424 (2015).

[56] S. Barkhofen, T. Nitsche, F. Elster, L. Lorz, A. Gábris, I. Jex, and C. Silberhorn, Phys. Rev. A **96**, 033846 (2017).

[57] F. Cardano, M. Maffei, F. Massa, B. Piccirillo, C. De Lisio, G. De Filippis, V. Cataudella, E. Santamato, and L. Marrucci, Nat. Commun. **7**, 11439 (2016).

[58] E. Flurin, V. V. Ramasesh, S. Hacohen-Gourgy, L. S. Martin, N. Y. Yao, and I. Siddiqi, Phys. Rev. X **7**, 031023 (2017).

[59] K. Mochizuki, D. Kim, and H. Obuse, Phys. Rev. A **93**, 062116 (2016).

[60] L. Xiao, X. Zhan, Z. H. Bian, K. K. Wang, X. Zhang, X. P. Wang, J. Li, K. Mochizuki, D. Kim, N. Kawakami, W. Yi, H. Obuse, B. C. Sanders, and P. Xue, Nat. Phys. **13**, 1117 (2017).

[61] A. Schreiber, K. N. Cassemiro, V. Potoček, A. Gábris, P. J. Mosley, E. Andersson, I. Jex, and C. Silberhorn, Phys. Rev. Lett. **104**, 050502 (2010).

[62] A. Crespi, R. Osellame, R. Ramponi, V. Giovannetti, R. Fazio, L. Sansoni, F. De Nicola, F. Sciarrino, and P. Mataloni, Nat. Photonics **7**, 322 (2013).

[63] A. Schreiber, K. N. Cassemiro, V. Potoček, A. Gábris, I. Jex, and C. Silberhorn, Phys. Rev. Lett. **106**, 180403 (2011).

[64] T. Kitagawa, M. A. Broome, A. Fedrizzi, M. S. Rudner, E. Berg, I. Kassal, A. Aspuru-Guzik, E. Demler, and A. G. White, Nat. Commun. **3**, 882 (2012).

[65] C. Chen, X. Ding, J. Qin, Y. He, Y.-H. Luo, M.-C. Chen, C. Liu, X. L. Wang, W. J. Zhang, H. Li, L. X. You, Z. Wang, D. W. Wang, B. C. Sanders, C. Y. Lu, and J. W. Pan, Phys. Rev. Lett. **121**, 100502 (2018).

[66] T. Nitsche, T. Geib, C. Stahl, L. Lorz, C. Cedzich, S. Barkhofen, R. F. Werner, and C. Silberhorn, New J. Phys. **21**, 043031 (2019).

[67] M. A. Broome, A. Fedrizzi, B. P. Lanyon, I. Kassal, A. Aspuru-Guzik, and A. G. White, Phys. Rev. Lett. **104**, 153602 (2010).

[68] X.-Y. Xu, Q.-Q. Wang, W.-W. Pan, K. Sun, J.-S. Xu, G. Chen, J.-S. Tang, M. Gong, Y.-J. Han, C.-F. Li, and G.-C. Guo, Phys. Rev. Lett. **120**, 260501 (2018).

[69] M. Karski, L. Förster, J.-M. Choi, A. Steffen, W. Alt, D. Meschede, and A. Widera, Science **325**, 174 (2009).

[70] S. Mugel, A. Celi, P. Massignan, J. K. Asbóth, M. Lewenstein, and C. Lobo, Phys. Rev. A **94**, 023631 (2016).

[71] Z. Yan, Y.-R. Zhang, M. Gong, Y. Wu, Y. Zheng, S. Li, C. Wang, F. Liang, J. Lin, Y. Xu *et al.*, Science **364**, 753 (2019).

[72] V. V. Ramasesh, E. Flurin, M. Rudner, I. Siddiqi, and N. Y. Yao, Phys. Rev. Lett. **118**, 130501 (2017).

[73] P. Xue, B. C. Sanders, and D. Leibfried, Phys. Rev. Lett. **103**, 183602 (2009).

[74] F. Zähringer, G. Kirchmair, R. Gerritsma, E. Solano, R. Blatt, and C. F. Roos, Phys. Rev. Lett. **104**, 100503 (2010).

[75] D. Leibfried, R. Blatt, C. Monroe, and D. Wineland, Rev. Mod. Phys. **75**, 281 (2003).
[76] R. Blatt and C. F. Roos, Nat. Phys. **8**, 277 (2012).
[77] J. Eisert, M. Friesdorf, and C. Gogolin, Nat. Phys. **11**, 124 (2015).
[78] J. Zhang, G. Pagano, P. W. Hess, A. Kyprianidis, P. Becker, H. Kaplan, A. V. Gorshkov, Z.-X. Gong, and C. Monroe, Nature (London) **551**, 601 (2017).
[79] J. Zhang, P. Hess, A. Kyprianidis, P. Becker, A. Lee, J. Smith, G. Pagano, I.-D. Potirniche, A. C. Potter, A. Vishwanath, N. Y. Yao, and C. Monroe, Nature (London) **543**, 217 (2017).
[80] T. Oka, N. Konno, R. Arita, and H. Aoki, Phys. Rev. Lett. **94**, 100602 (2005).
[81] C. Ospelkaus, U. Warring, Y. Colombe, K. Brown, J. Amini, D. Leibfried, and D. J. Wineland, Nature (London) **476**, 181 (2011).
[82] J. L. Sørensen, D. Møller, T. Iversen, J. B. Thomsen, F. Jensen, P. Staanum, D. Voigt, and M. Drewsen, New J. Phys. **8**, 261 (2006).
[83] Y. Wu and X. Yang, Phys. Rev. Lett. **78**, 3086 (1997).
[84] D. Lv, S. An, Z. Liu, J.-N. Zhang, J. S. Pedernales, L. Lamata, E. Solano, and K. Kim, Phys. Rev. X **8**, 021027 (2018).
[85] B. E. King, C. S. Wood, C. J. Myatt, Q. A. Turchette, D. Leibfried, W. M. Itano, C. Monroe, and D. J. Wineland, Phys. Rev. Lett. **81**, 1525 (1998).
[86] C. Wunderlich, T. Hannemann, T. Körber, H. Häffner, C. Roos, W. Hänsel, R. Blatt, and F. Schmidt-Kaler, J. Mod. Opt. **54**, 1541 (2007).
[87] F. Gebert, Y. Wan, F. Wolf, J. C. Heip, and P. O. Schmidt, New J. Phys. **18**, 013037 (2016).
[88] M. Um, J. Zhang, D. Lv, Y. Lu, S. An, J.-N. Zhang, H. Nha, M. Kim, and K. Kim, Nat. Commun. **7**, 11410 (2016).
[89] B. Simon, Phys. Rev. Lett. **51**, 2167 (1983).
[90] K. Bergmann, H. Theuer, and B. W. Shore, Rev. Mod. Phys. **70**, 1003 (1998).
[91] M. V. Berry, J. Phys. A: Math. Theor. **42**, 365303 (2009).
[92] X. Chen, I. Lizuain, A. Ruschhaupt, D. Guéry-Odelin, and J. G. Muga, Phys. Rev. Lett. **105**, 123003 (2010).
[93] Y.-X. Du, Z.-T. Liang, Y.-C. Li, X.-X. Yue, Q.-X. Lv, W. Huang, X. Chen, H. Yan, and S.-L. Zhu, Nat. Commun. **7**, 12479 (2016).
[94] M. Sajid, J. K. Asbóth, D. Meschede, R. F. Werner, and A. Alberti, Phys. Rev. B **99**, 214303 (2019).
[95] T. Li, Y.-S. Zhang, and W. Yi, Chin. Phys. Lett. **38**, 030301 (2021).
[96] C. Zener, Proc. R. Soc. London Ser. A **137**, 696 (1932).